Maladaptive nutrient signalling sustains the m.3243A>G mtDNA mutation

Chih-Yao Chung[1], Kritarth Singh[1], Vassilios N Kotiadis[1], Jee Hwan Ahn[1], Lida Kabir[1], Emilie Topley[1], Joycelyn Tan[1], William D Andrews[1], Nicoletta Plotegher[1,2], Graziano Guella[3], Robert D S Pitceathly[4], Gyorgy Szabadkai[1,5,6], Mariia Yuneva[6], Michael R Duchen[1*]

1 Department of Cell and Developmental Biology and Consortium for Mitochondrial Research, UCL, Gower Street, London WC1E 6BT

2 Department of Biology, University of Padua, Padua, Italy

3 Bioorganic Chemistry Laboratory, Department of Physics, University of Trento, Trento, Italy

4 Department of Neuromuscular Diseases, UCL Queen Square Institute of Neurology and The National Hospital for Neurology and Neurosurgery

5 Department of Biomedical Sciences, University of Padua, Padua, Italy

6 The Francis Crick Institute, London

*Correspondence: m.duchen@ucl.ac.uk

Keywords: mitochondria; mtDNA; mtDNA mutations; nutrient signalling; m.3243A>G; PI3K; Akt; mTORC1; mitophagy

ABSTRACT

Mutations of the mitochondrial genome (mtDNA) cause a range of profoundly debilitating clinical conditions for which treatment options are limited. Most mtDNA diseases show heteroplasmy – tissues express both wild-type and mutant mtDNA. The relationships between specific mtDNA mutations, heteroplasmy, disease phenotype and severity are poorly understood. We have extensively characterised changes in bioenergetic, metabolomic, lipidomic and RNAseq profiles in heteroplasmic patient-derived cells carrying the m.3243A>G mtDNA mutation, the cause of mitochondrial encephalomyopathy, lactic acidosis and stroke-like episodes (MELAS). These studies reveal that the mutation promotes upregulation of the PI3K-Akt-mTORC1 axis in patient-derived cells and tissues. Remarkably, pharmacological inhibition of PI3K, Akt, or mTORC1 activated mitophagy, reduced mtDNA mutant load and rescued cellular bioenergetics cell-autonomously. The rescue was prevented by inhibition of mitophagy. These findings suggest that activation of the PI3K-Akt-mTORC1 axis is maladaptive and represents a potential therapeutic target for people suffering from the consequences of the m.3243A>G mutation.

INTRODUCTION

Mitochondria control cellular bioenergetic homeostasis and serve as a hub for cell metabolism and cell signalling pathways. Human mitochondria contain a circular plasmid-like DNA (mtDNA) which encodes 13 proteins which act as subunits of the electron transport chain (ETC) and 24 RNAs essential for mitochondrial protein synthesis. Mutations of mtDNA affect around 1 in 5000 of the population[1] and cause a range of diseases for which no effective treatment is available[2,3]. Over half of the known pathogenic mutations are found within tRNA genes, in which the m.3243A>G mutation, a $tRNA^{Leu}$ point mutation accounts for about 40% of adult patients of primary mitochondrial diseases[1,4]. Clinically, patient symptoms associated with mtDNA mutations are highly heterogeneous[2,5]. The tissues primarily affected vary depending on the specific mtDNA mutations, and our understanding of the relationships between mtDNA mutations, disease phenotype and severity is still very limited[2,3]. The majority of diseases caused by mutations of mtDNA are heteroplasmic – tissues express both normal and mutation carrying mtDNA. This is a confounding complication, as disease expression may differ radically between patients with the same mutation but different mutant load. While disease severity broadly correlates positively with the relative burden of mutant mtDNA, we know remarkably little about the determinants of the mutant mtDNA burden[3,6–8].

Mitochondrial quality control pathways, including mitophagy, mitochondrial biogenesis pathways and mitochondrial shaping mechanisms, are critically involved in regulating mitochondrial energy homeostasis[9,10]. Several studies have demonstrated the accumulation of damaged mitochondria and defective mitophagy as a hallmark of mtDNA diseases and age-related neurodegeneration, suggesting that the presence of pathogenic mtDNA alone is not sufficient to drive selection against the mutation by the activation of mitophagy[11–15]. We therefore asked how cell signalling pathways influence these pathways in the disease model, as adaptive - or maladaptive – responses to impaired oxidative phosphorylation (OxPhos) and changes in intermediary metabolism, and whether these pathways play a role as determinants of mutant load and disease severity.

Here, we have characterised the metabolic phenotype of patient-derived cells bearing the m.3243A>G ($tRNA^{Leu}$) mutation. This is the most common heteroplasmic mtDNA mutation[1,4], and, clinically, is expressed variably but may include diabetes, sensorineural deafness, myopathy, encephalopathy, lactic acidosis and stroke-like episodes (MELAS). We have found that the expression and activity of the PI3K-Akt-mTORC1 pathway were increased in the mutant cells, and was strongly associated with redox imbalance, oxidative stress, and glucose dependence. Phosphorylation of Akt and ribosomal protein S6 (a downstream target of mTORC1) were also increased in muscle biopsies from other patients with the mutation, confirming that this signalling pathway is constitutively activated in

patient tissues. Remarkably, inhibition of PI3K, Akt, or mTORC1 all substantially reduced mutant load and rescued mitochondrial bioenergetic function. We found that this process is mediated by upregulation of mitophagy which is absolutely required for rescue of mitochondrial function and reduction in mutant load. Our study reveals that in response to the m.3243A>G mutation, metabolism is rewired, and activity of the PI3K-Akt-mTORC1 axis is increased, as an adaptive response to metabolic changes driven by the mutation. The finding that inhibition of the pathway reduces mutant load and rescues function suggests that activation of this signalling pathway is, in fact, maladaptive, that activation of the pathway sustains disease progression and that pharmacological intervention in this signalling pathway represents a potential therapeutic strategy in patients with these dreadful diseases.

RESULTS

The m.3243A>G mutation causes mitochondrial dysfunction and glucose dependence, resulting in redox imbalance and oxidative stress.

To explore the metabolic and cell signalling impact of the m.3243A>G mutation, we used six cell lines: fibroblasts derived from two patients carrying the mutation, two controls matched for age and gender, an A549 cybrid cell line carrying the mutation and its Wild-type (WT) counterpart. PCR-RFLP[16] and ARM-qPCR[17] were used to quantify the m.3243A>G mutation load in these cell models. One patient-derived line (henceforth referred to as patient 1) showed a mutant load of 86.2 ± 2.3%; a second line (referred to as patient 2) showed a mutant load of 30.3 ± 3.5%, and the mutant load was 79.0 ± 0.3% in the cybrid cells (Fig. 1A; for more details about the patients please see Methods).

To characterise the metabolic phenotype of the mutant cells, respiratory rate was measured using the Seahorse XFe96 extracellular flux analyser. These measurements showed a profound decrease in resting respiratory rate, ATP dependent respiration and in maximal respiratory capacity in both patient lines (Fig. 1B, D). Respiratory rates were also significantly reduced in the cybrid cells, when normalised to their increased mtDNA copy number (Fig. S1A), compared to the control A549 cells (Fig. 1C-D). In line with these findings, immunoblotting of respiratory chain supercomplexes using blue native gels electrophoresis (BNGE), which identify macromolecular assemblies, revealed disrupted expression of respiratory chain proteins in the mutant cells (Fig. 1E). Notably, there was a very large decrease in supercomplex I_2+ III_2 +IV_n, III_2+IV_1 and III_2/IV_2 assembly and in complex IV_1 (Fig. 1E). Mitochondrial membrane potential ($\Delta\psi_m$) was reduced in both patient-derived fibroblast lines (Fig. 1F) and the cybrid cells (Fig. S1B). The decrease in $\Delta\psi_m$ was significantly greater in cells from patient 1 than from patient 2, consistent with the greater mutant load in patient 1. Mitochondrial morphology was also altered in patient fibroblasts, showing significant fragmentation of the mitochondrial network, which was more severe in cells from patient 1 than from patient 2 (Fig. 1F).

Mitochondrial dysfunction may alter rates of free radical generation by the respiratory chain. The rate of increase of dihydroethidium (DHE) fluorescence (Fig. S1C), reflecting the intracellular rate of production of reactive oxygen species (ROS), was significantly increased both in patient fibroblasts and in the cybrid cells, compared to matched controls (Fig. 1G and S1D). MitoSOX, a mitochondria-targeted form of DHE, revealed a significant increase in the rate of ROS generation in the mitochondria in the mutant cells (Fig. 1G, ii; Fig. S1D, ii), suggesting that the increased rate of ROS generation is likely the consequence of an impaired respiratory chain. Together, the m.3243A>G mutation results in mitochondrial dysfunction, mitochondrial fragmentation and elevated ROS generation.

106 We wondered whether glucose metabolism is altered in the mutant cells, supporting their
107 bioenergetic homeostasis and compensating for the mitochondrial dysfunction. Using time-lapse live-
108 cell imaging, we quantified cell growth rates by fitting the curves of cell confluence with an exponential
109 cell growth model (Fig. S1E) under a variety of nutrient conditions. Growth rates were significantly
110 reduced in all mutant fibroblasts compared to their control counterparts (Fig. S1F). Moreover, the cell
111 proliferation rate was significantly reduced in all mutant cells in 1 and 5 mM glucose media (Fig. 1H
112 and S1G) but not in low concentrations of glutamine, suggesting that the patient-derived cells are
113 significantly more dependent on glucose metabolism. Consistently, the rate of uptake of the
114 fluorescent glucose analogue, 2-NBDG, was significantly increased in both patient fibroblasts and the
115 cybrid cells, compared to controls (Fig. 1I and S1H).

116 The cytosolic NADH:NAD^+ ratio is a function of glycolytic flux (which consumes NAD^+, generating
117 NADH), lactate production through lactate dehydrogenase (LDH) which produces lactate and
118 regenerates NAD^+ from NADH and the activity of malate/aspartate and the glycerol phosphate
119 shuttles that exchange NADH and NAD^+ between cytosol and mitochondrial matrix (Fig. 1J). We used
120 the genetically encoded reporter SoNar[18] to quantify the cytosolic NADH:NAD^+ ratio (Fig. S1I). The
121 basal NADH:NAD^+ ratio was significantly increased in the patient fibroblasts and cybrid cells compared
122 to controls, consistent with reduced mitochondrial activity and higher glucose catabolism through
123 glycolysis (Fig. 1K and S1J). It was also consistent with significantly higher levels of lactate produced
124 by the patient fibroblasts compared to controls (Fig. 1L). The pH of the growth media, reflecting
125 cellular lactate production, was also measured using the absorbance of phenol red. The acidification
126 of media by mutant cells was significantly greater than that of controls (Fig S1K). These data
127 recapitulate the lactic acidosis which is characteristic of patients with the m.3243A>G mutation[19], and
128 suggest that in patient fibroblasts, increased activity of LDH may compensate for the decreased
129 regeneration of NAD^+ by mitochondria, supporting increased glycolytic flux. Addition of exogenous
130 pyruvate can support mitochondrial activity, increasing OxPhos, and stimulate LDH activity to generate
131 lactate, changing the NADH:NAD^+ ratio. In control cells, pyruvate addition decreased the cytosolic
132 NADH:NAD^+ ratio, but had a negligible effect on the high NADH:NAD+ ratio in mutant cells (Fig. 1K and
133 S1J), suggesting that in the latter, LDH flux is already operating at its maximum capacity. Together,
134 these data confirm that in the mutant cells, decreased mitochondrial activity results in higher glucose
135 uptake, glucose catabolism into lactate and increased cytosolic NADH:NAD^+ ratio.

136

137 **The m.3243A>G mutation remodels glucose and lipid metabolism towards increased anabolic**
138 **biosynthesis and lipid accumulation.**

139 To investigate the glucose-dependent metabolic alterations in the mutant cells and identify metabolic
140 signals which might result in cell signalling changes, glucose uniformly labelled with isotopic carbon
141 ([U-^{13}C]-glucose) was used to trace its metabolic fate in the cells by gas chromatography-mass
142 spectrometry (GC-MS). The pattern and abundance of ^{13}C enrichment in downstream metabolites
143 were used to determine the relative contribution of glucose into different metabolic pathways. First,
144 partial least squares discriminant analysis (PLS-DA) for the concentration of metabolites (Fig. S2A)
145 showed a clear separation between patient fibroblasts and controls (Fig. S2B). The analysis of
146 metabolic pathways revealed enrichment of lipid metabolism, pentose phosphate pathway (PPP),
147 glycolysis and the tricarboxylic acid (TCA) cycle (Fig. 2A). Tracing the fate of ^{13}C-glucose through
148 glycolysis (Fig. 2B), we found that the enrichment of ^{13}C in glucose-6-phosphate (G6P) in the mutant
149 cells was at a similar level as in controls (Fig 2B), but the total pools of G6P were increased (Fig. S2A)
150 consistent with increased glucose uptake. Although the end products of glycolysis, intracellular pools
151 of pyruvate and lactate in the mutant cells, were maintained at similar levels with controls in terms of
152 ^{13}C enrichments and concentrations (Fig. 2B and S2A), the levels and the ^{13}C enrichment of glycerol-3-
153 phosphate (G3P) were increased. The latter suggests the increased activity of glycerol-3-phosphate
154 dehydrogenase in response to increased cytosolic NADH/NAD$^+$ ratio, which may drive elevated lipid
155 biosynthesis (Fig. 2B). Interestingly, the levels of alanine were increased but its ^{13}C enrichment was
156 decreased, suggesting a contribution from other nutrient sources. Similarly, the total amount of serine
157 was increased in patient fibroblasts, despite decreased synthesis of serine from glucose, suggesting
158 increased serine uptake from extracellular media (Fig. 2B, S2A and S2C).

159 Consistent with OxPhos defects, levels of the TCA cycle intermediates, malate, fumarate and
160 succinate, were decreased in the mutant cells, while the levels of citrate were increased (Fig. S2A).
161 Interestingly, the enrichment of m+3 isotopologues of these TCA cycle intermediates and aspartate
162 were significantly increased in the mutant cells (Fig. 2B). To enter the TCA cycle, glucose-derived
163 pyruvate is converted into acetyl-CoA by pyruvate dehydrogenase (PDH). In this case the catabolism
164 of [U-^{13}C]-glucose results in m+2 enrichment of TCA cycle intermediates, including oxaloacetate (OAA),
165 a precursor of aspartate. In contrast, m+3 isotopologues of TCA cycle intermediates are generated if
166 pyruvate is converted into OAA by pyruvate carboxylase (PC). Metabolite set enrichment analysis of
167 the metabolomics data also predicted that PC is affected (Fig. S2D). Immunoblotting for phospho-PDH
168 and PC expression revealed elevated PC expression and increased levels of phosphorylated PDH
169 (indicating its reduced activity) in both patient fibroblasts and cybrid cells (Fig. 2C). As the glucose
170 contribution into the TCA cycle is usually low in conventional cell culture systems, this slight but
171 significant difference in the enrichment of ^{13}C is meaningful. The switch from PDH to PC as means of
172 channelling glucose-derived carbon into the TCA cycle in mutant fibroblasts is consistent with the

173 increased NADH/NAD+ ratio, which stimulates the activity of pyruvate dehydrogenase kinase,
174 phosphorylating PDH and inhibiting its activity.

175 As increased levels and glucose-derived enrichment of G3P suggest increased lipid biosynthesis, we
176 asked whether lipid metabolism is altered in the mutant cells. Nile Red O staining, which labels neutral
177 lipids, showed a substantial and significant accumulation of lipid droplets in the mutant cells,
178 increasing both the number and the area of droplets (Fig. 2D). Interestingly, accumulation of lipid
179 droplets has also been seen in biopsies from patients with MELAS[20]. A systematic lipidomic analysis
180 using LC-MS showed that lipid profiles of patient fibroblasts were distinct from the controls, with a
181 striking increase in membrane and storage lipids, including glycerophosphatidylinositols, cholesteryl
182 esters and sphingomyelins (Fig. 2E). PLS-DA again showed a clear separation of lipidomic profile
183 between patient and control fibroblasts (Fig. S2E). Similarly, the enrichment of metabolic pathways
184 from the lipidomic data revealed upregulation of processes involved in membrane lipid metabolism
185 and signalling systems (Fig. S2F). Our findings from the stable-isotope-labelling approach and
186 comparative metabolomics thus reveal a profound remodelling of glucose and lipid metabolism as a
187 consequence of OxPhos defects arising from the m.3243A>G mutation.

188

189 **The chronic activation of PI3K-Akt-mTORC1 in the m.3243A>G mutant cells impairs autophagy and**
190 **induces a deleterious integrated stress response**

191 The metabolic phenotype shown above points to reprogramming of nutrient-sensing signalling
192 networks in the m.3243A>G mutant cells. We therefore carried out an RNA sequencing screen to
193 examine global changes in the expression profiles of the patient fibroblasts. Using a significance level
194 of false discovery rate (FDR) < 0.05, we identified 3394 transcripts of which 1849 were upregulated
195 and 1545 were downregulated. A multi-dimensional principal component analysis also confirmed
196 good accordance between biological triplicates as well as close clustering of transcripts from patient
197 fibroblasts (Fig. S3A-C). The enrichment analysis of these differentially expressed genes identified
198 'mitochondrial dysfunction', 'superoxide radical degradation', 'Cholesterol biosynthesis' as the top-
199 scoring pathways in patient fibroblasts (Fig. 3A). Analysis of individual genes involved in these
200 pathways showed a general downregulation of OxPhos genes (Fig. S3D), but increased expression of
201 genes involved in oxidative stress defence pathways and membrane lipid synthesis/remodelling (Fig.
202 S3E-F). Specifically, the increased expression of PC was consistent with the immunoblotting data (Fig.
203 2C) and correlated with altered TCA cycle activity (Fig. S3G). The enhancement of glycolytic flux in the
204 mutant cells reported by the metabolomic data was supported by the increased expression of

205 hexokinase 1 (HK1). These findings further validated the metabolic footprint observed in patient-
206 derived cells from the metabolomic studies.

207 Consistent with the above results, the network analysis of upregulated genes identified the strong
208 enrichment of NRF2 signalling as well as PI3K-Akt and mTOR pathways in patient fibroblasts (Fig. 3B
209 and Fig. S4A; Table S1). We next validated these data at the protein expression level. Immunoblotting
210 confirmed increased phosphorylation of Akt compared to total Akt, as well as the downstream
211 mTORC1 target S6 ribosomal protein in patient fibroblasts (Fig. 3C) and the cybrid cells (Fig. S4B).
212 While control fibroblasts showed a growth factor-dependent Akt activation in response to increased
213 serum concentration in growth media, phospho-Akt was elevated in patient cells even when growth
214 factors were low (1% FBS) and increased only slightly in response to an elevated serum concentration.
215 Similarly, the patient fibroblasts exhibited increased mTORC1 activation independently of the serum
216 concentration, revealed by increased phospho-S6 levels. PI3K-Akt-mTORC1 signalling also antagonizes
217 the activity of the cellular energy sensor, AMP-activated protein kinase (AMPK) and suppresses
218 macromolecular catabolism by autophagy. We therefore measured AMPK phosphorylation in
219 response to different serum concentration by immunoblotting, but found no significant difference
220 between patient and control fibroblasts. These results suggest that the constitutive induction of PI3K-
221 Akt-mTORC1 signalling remodels cell metabolism, independently of growth factor stimulation.

222 We next explored the impact of chronic induction of PI3K-Akt-mTORC1 signalling on autophagic flux
223 in the mutant cells (Fig. 3D)[13,21]. We monitored LC3B turnover in the presence and absence of
224 chloroquine (CQ) using LC3B immunoblotting. The mutant cells showed an increased conversion to
225 LC3BI to LC3BII form (autophagosome) but the difference in LC3BII accumulation in the presence of
226 CQ was not significantly different between control and mutant cells (Fig. 3E and S4C), indicating a
227 defect in the late stage of autophagosome to autolysosome conversion/fusion in mutant cells. We
228 also measured the autophagic flux using a mCherry-EGFP-LC3B tandem reporter[22] by live-cell imaging.
229 Consistent with the above result, the ratio of green/red puncta was low in control compared to patient
230 cells, representing the formation of mature autolysosomes and a high autophagy flux. In contrast, the
231 ratio of green/red puncta and both the number and size of double-positive puncta were increased in
232 mutant cells, indicating impaired autophagosome maturation into autolysosomes (Fig. 3F and S4D).
233 Altogether, these results confirm that autophagic flux is impaired in the mutant cells and further
234 indicate that an autophagy imbalance may contribute to metabolic and proteostatic stress in PI3K-
235 Akt-mTORC1 activated cells.

236 Indeed, the network analysis of downregulated genes identified EIF2 and PTEN signalling as the top
237 downregulated pathways (Fig. 3B). PTEN is a negative regulator of the PI3K-Akt-mTORC1 axis.
238 Interestingly, inhibition of EIF2 signalling, a hub for the integrated stress response (ISR) and regulation

239 of protein translation under stress, in the m.3243A>G mutant cells indicated an attenuation of protein
240 synthesis and induction of ISR[23,24]. Analysis of the individual transcripts from EIF2 signalling pathway
241 showed a general downregulation of genes involved in ribosomal biogenesis and upregulation of
242 transcription factors – ATF4, ATF5 and DDIT3 (CHOP) (Fig. S4A; Table S2-3). ATF4 acts as a prototypical
243 downstream target coupling mitochondrial proteotoxic stress to the activation of ISR[25]. We therefore
244 examined the protein expression levels of these genes to demonstrate the activation of the ISR in
245 patient-derived cells. A significant increase in the phosphorylation levels of translation factor, eIF2α
246 as well as the downstream targets, ATF4, ATF5 and CHOP confirmed the induction of the ISR in the
247 mutant cells (Fig. 3G and Fig. S4E).

248 To establish that the PI3K-Akt-mTORC1 axis is constitutively active in patients with the m.3243A>G
249 mtDNA mutation, we measured p-Akt/Akt and p-S6/S6 by immunofluorescence in a muscle biopsy
250 from a patient with an 82% mutant load of the m.3243A>G mutation causing MELAS, (not one of the
251 donors used to obtain the fibroblasts). A significant increase in p-Akt and p-S6 in the muscle biopsy
252 argues that upregulation of this pathway is a clinical feature of the disease and not a specific function
253 of the cultured cells (Fig. 3H). Re-analysis of a published RNA-seq data set[26] from muscle biopsies of
254 MELAS patients also confirmed alterations in cholesterol and serine biosynthesis (Fig. 3I) and the
255 activation of PI3K-Akt-mTORC1 signalling and induction of ISR in patients (Table S4). Although
256 activation of the ISR has been proposed to be cytoprotective and promote longevity[27,28], our data
257 suggest that the activation of ISR in the context of the m.3243A>G mtDNA mutation is not protective.
258 Combined mitochondrial dysfunction, metabolic remodelling and impaired autophagy may act as an
259 overarching inducer of ISR in PI3K-Akt-mTORC1 activated m.3243A>G mutant cells[29].

260

261 **Pharmacological inhibition of PI3K-Akt-mTORC1 signalling reduces mutant load, resolves ISR,**
262 **rescues mitochondria function and lowers glucose dependence in the m.3243A>G mutant cells**

263 At this point, we asked what the functional consequences of the activation of the PI3K-Akt-mTORC1
264 axis are and whether it represents an adaptation to impaired OxPhos. We therefore systematically
265 inhibited each component of the axis in turn using well-established pharmacological inhibitors (Fig.
266 4A)[21] and explored the consequences for mutant mtDNA burden and the pathophysiological and
267 biochemical features that we have described above.

268 In both the fibroblasts from patient 1 and the cybrid cells, treatment with LY294002 (referred to below
269 as 'LY', 5 μM, an inhibitor of PI3K) or with rapamycin (referred to as 'RP', 5 μM, the canonical inhibitor
270 of mTORC1) led to a progressive decrease in mutant mtDNA load over 12 weeks of sustained
271 treatment (Fig. 4B). The efficacy of each drug as the inhibitor of the PI3K-Akt-mTORC1 axis was

272 confirmed by immunoblotting the downstream kinase targets, showing significant changes in
273 phosphorylated to unphosphorylated forms. Interestingly, in the absence of RP or LY, the fibroblasts
274 from patient 2 showed a progressive increase in mutant load with time in culture, rising from ~30% to
275 around 70% over 3 months (Fig. 4B). Treatment with the inhibitors significantly suppressed the rate
276 of increase in mutant load decreasing the total change by around 20%. Although the decrease in
277 mutant load took many weeks to develop, changes in protein phosphorylation state were evident
278 within a day of starting treatment (Fig. 4C and S5A). Accordingly, inhibition of PI3K by LY reduced p-
279 Akt/Akt ratio and mTOR phosphorylation, while rapamycin inhibited mTOR phosphorylation but had
280 no impact on Akt. None of the treatments had any immediate effect on AMPK phosphorylation.
281 However, AMPK activity gradually increased at later time points after drug treatments, suggesting an
282 induction of catabolic processes such as autophagy and improvement in sensing the bioenergetic
283 status of the m.3243A>G mutant cells[30]. The ISR/UPR^{mt} pathway also changed accordingly after the
284 drug treatments (Fig. 4C and S5B), which restored the expression of ATF4 and ATF5 to levels that were
285 comparable to that of control. In LY-treated cells, ATF4 and ATF5 were downregulated almost
286 immediately, while, interestingly, in RP-treated cells, ATF4 and ATF5 were decreased after a week of
287 treatment. These data confirmed that the PI3K-Akt-mTORC1 axis is an upstream regulator of ISR[23,31],
288 although the mechanisms by which inhibition of mTORC1 or PI3K/Akt resolves the ISR may differ[29].

289 To investigate whether the decrease in mutant load and suppression of ISR after drug treatment were
290 reflected by a concomitant change in mitochondrial function, we measured the mitochondrial
291 bioenergetic status and the metabolic phenotype of the patient-derived cells. Measurements of
292 mitochondrial membrane potential showed a complete recovery to levels that were not significantly
293 different from control cells (Fig. 4D and S5C). These changes were accompanied by a decrease in the
294 fragmented phenotype in the mutant cells and a significant elongation and reformation of a
295 mitochondrial network (Fig. 4D and S4C). Measurements of mitochondrial respiration showed that
296 both basal and maximal respiratory capacity were increased in cells treated with LY or RP (Fig. 4E and
297 S5D). Treatment of mutant cells with MK2206 (MK, 1 μM), a pan Akt inhibitor, also caused a
298 progressive decrease in mutation load and restored mitochondrial function (Fig. S5E-I). We also
299 examined the effects of LY and RP in cells carrying another heteroplasmic mtDNA point mutation –
300 the m.8993T>G – generated by the Minczuk lab[27]. In these cells, inhibition of the PI3K-Akt-mTORC1
301 axis had no impact on mutant load (Fig. S5J), suggesting that hyperactivation of the PI3K-Akt-mTORC1
302 axis is relatively disease specific.

303 The improvement in mitochondrial respiration suggested a metabolic shift towards OxPhos.
304 Measurements of cytosolic redox state using SoNar (Fig. 4F and S5K) showed a significant reduction
305 in basal NADH:NAD$^+$ ratio and increased response to pyruvate addition in the long-term treated

306 patient-derived cells, implying a decreased glycolytic flux. Measurements of glucose and lactate
307 concentration in the media showed a profound decrease in lactate secretion following LY and RP
308 treatments (Fig 4G and S5L). The cells were also cultured in media containing glucose or galactose as
309 a primary carbon source to further assess their dependence on glycolysis. LY- and RP-treated cells, but
310 not mutant controls, grew well in the galactose media, indicating a reduced glycolytic dependence
311 after the drug treatments (Fig. 4H). Also, the mutant cells showed an increased supercomplex
312 formation as well as individual components of the mitochondrial ETC following drug treatments (Fig.
313 4I). In Gel activity assay for CI and CIII+CIV revealed a significant increase in enzyme activity of ETC in
314 response to the inhibitors (Fig. S5M). Further, the rates of ROS production were also reduced in cells
315 treated with LY and RP (Fig. 4J and S5N). Altogether, our results demonstrate that the long-term
316 treatment of the mutant cells with either LY or RP reverses the biochemical consequences of the
317 mutation, rescuing mitochondrial function, reducing glucose dependence and decreasing the
318 mutation load. These data strongly argue that the chronic activation of the PI3K-Akt-mTORC1 axis,
319 presumably as an adaptive response to impaired oxidative metabolism, instead serves as a
320 maladaptive response in this disease model.

321

322 **Reduction of the m.3243A>G mutant load by inhibition of the PI3K-Akt-mTORC1 axis is cell-**
323 **autonomous**

324 The chronic activation of the PI3K-Akt-mTORC1 axis and increased mutant load have deleterious
325 effects on cellular function and amplify the pathophysiological consequences of the mutation.
326 However, this raises questions about the underlying mechanism by which inhibition of the axis reduces
327 mutant load and rescues mitochondrial function. A possible explanation for the response to drug
328 treatments is that inhibition of the signalling pathway may promote the selective growth of cell
329 populations with low mutant load or selective elimination of cells with high mutant loads. We
330 therefore carried out long term measurements of growth rates and cell death (Fig. 5A, i and ii).
331 Although treatment with either LY or RP significantly slowed cell proliferation in both fibroblast and
332 cybrid cells (Fig. 5B, upper panel), the changes were small. The cell growth rate was stable in cybrid
333 cells treated with LY or RP, suggesting that there was no clonal expansion. In fibroblasts, growth rates
334 of cells were not altered by treatment with drugs for 4 or 8 weeks, while a significant decrease of
335 mutation load was clearly established after 4 weeks of treatment. This suggests that the change of
336 mutation load is independent of the rate of cell growth. Cell death rates in the drug-treated groups
337 were even lower than in the mutant controls, suggesting that the drug treatments were beneficial,
338 and there was no selective killing of mutant cells (Fig. 5B, lower panel). Treating the mutant cells with
339 MK showed similar results in terms of cell growth and death (Fig. S5A).

340 To determine definitively whether the reduction of mutant load in response to the drug treatments is
341 cell-autonomous, we used a PCR-based technique, TaqMan SNP genotyping, at single-cell resolution
342 to measure the distributions of the m.3243A>G heteroplasmy in a cell population (Fig. 5Aiii). The
343 TaqMan technique was first validated by measuring the mutation loads of a population of cells and
344 then to establish the range of single-cell mutant load across the population (Fig. S6B). The distribution
345 of mutant load in the cybrid cells ranged from 50-80%, showing a Gaussian distribution (Fig. S6C). The
346 average single-cell mutant load was consistent with that of the whole cell population. Measurement
347 of the relative m.3243A>G heteroplasmy in patient fibroblasts and cybrid cells following treatment
348 with LY and RP for 6 and 12 weeks respectively showed a frequency distribution which clearly
349 segregated the treated group as a distinct population from the untreated group (Figs. 5C-D). The
350 distribution of the mutant load in treated groups, although showing stochastic variation within the
351 population, shifted to significantly lower levels compared to the untreated group. To determine
352 whether the reduction in the burden of the m.3243A>G heteroplasmy is also phenocopied at the
353 protein expression level, we immunostained the mtDNA-encoded cytochrome c oxidase I (MT-COI) in
354 patient 1 fibroblasts. The presence of 7 UUA-encoded leucine residues within MT-COI renders the
355 m.3243A>G $tRNA^{Leu(UUR)}$ cells prone to codon-specific translational defect[32]. Immunofluorescence
356 staining revealed a significant decrease in MT-COI expression in patient 1 fibroblasts compared to
357 controls (Fig. S6D). Following drug treatments, these cells showed a partial but significant recovery of
358 MT-COI expression. The single-cell analysis of MT-COI expression segregated the drug-treated and
359 untreated groups in a distribution pattern similar to the m.3243A>G proportion in Fig. 5D. A
360 diminished expression of MT-COI also correlated with the lower assembly and activity of
361 supercomplexes in Fig. 4I. Together, these results strongly suggest that rather than the enrichment of
362 a specific cell population, the reduction in m.3243A>G heteroplasmy caused by inhibition of PI3K-Akt-
363 mTORC1 signalling operates across the whole population and is likely cell-autonomous.

364

365 **Restoration of autophagic/mitophagic flux by PI3K-Akt-mTORC1 inhibition is necessary to reduce**
366 **the m.3243A>G mutant load.**

367 Our results from the single-cell analysis strongly argue that the change in heteroplasmy is a cell-
368 autonomous phenomenon. We then asked what mechanisms select against the mutant mtDNA. A
369 possible explanation could be the elimination of the mutant mtDNA by reducing the total mtDNA copy
370 number and then amplifying the dominant mtDNA, resembling 'the bottleneck' effect – the selection
371 mechanism of mtDNA in germline or embryo[4,6]. We therefore quantified the total mtDNA copy
372 number of the drug-treated cells at a series of time points, but no significant changes were seen

373 between the mutant control and drug-treated cells (Fig. S7A) and the total mtDNA copy number
374 remained stable across the duration of drug treatments.

375 It also seemed plausible that the removal of dysfunctional mitochondria via mitophagy may reduce
376 the mutant load in cells with the mtDNA mutation[33,34]. Indeed, long-term treatment with either RP or
377 LY significantly increased the conversion and accumulation of LC3BII (autophagosome) in the presence
378 of CQ compared to untreated cells (Fig. 6A and Fig. S7B). Notably, the autophagic flux, evident by a
379 high LC3BII/LC3BI ratio in the presence of CQ, increased progressively with time closely mirroring the
380 rate of decrease in mutant load (see Fig. 4B). Measurement of autophagic flux using the mCherry-GFP-
381 LC3 probe (Fig. 6B and Fig. S7C) showed a significant increase in the formation of autolysosomes (red
382 puncta) as early as 24 h of drug treatment and increased upon long-term treatment in patient
383 fibroblasts. Moreover, the ratio of green/red signal as well as the average puncta size decreased
384 significantly, suggesting the restoration of autophagy flux in the m.3243A>G mutant cells after drug
385 treatment.

386 To evaluate how the increased efficacy of autophagy affects mitophagy status, immunostaining of LC3
387 and cytochrome c was performed in the cybrid cells (Fig. S7D). The long-term drug treatment with RP
388 and LY dramatically increased the association between mitochondria and autophagosomes,
389 suggesting the restoration of mitophagy flux. To quantify mitochondrial degradation, we transfected
390 the cells with mitochondrial-targeted mKeima (mt-Keima, Addgene plasmid #56018), which
391 undergoes a spectral shift within acidic lysosomes. In control cells, the ratio of excitation (F_{543}/F_{458})
392 was high, demonstrating a differential distribution of intact (green) and degraded (red) mitochondria
393 (Fig. S7E), while in untreated patient fibroblasts, the fragmented mitochondrial network was evident,
394 and the proportion of high ratio (F_{543}/F_{458}) signal area to the total mitochondrial area was significantly
395 decreased, consistent with impaired mitophagic flux (Fig. 6C). However, after 24 h of drug treatments,
396 the (F_{543}/F_{458}) ratio increased with a concomitant increase in red puncta (degraded mitochondria) in
397 drug-treated patient fibroblasts. Altogether, these findings confirm that inhibition of PI3K-Akt-
398 mTORC1 signalling restores autophagy and promotes mitophagic flux in the m.3243A>G mutant cells

399 The progressive decrease in mutant load and increase in autophagic flux with time following PI3K-Akt-
400 mTORC1 inhibition in the m.3243A>G mutant cells strengthened the idea that upregulated mitophagic
401 flux drives selection against the mutant mtDNA and decreases the mutant load. To explore this further,
402 we quantified mitophagy in patient fibroblasts expressing mtKeima, cotreated with CQ in combination
403 with RP or LY. The cotreatment with CQ decreased the high ratio (F_{543}/F_{458}) signal to levels comparable
404 to untreated patient fibroblasts, indicating that the CQ treatment reversed the effect of LY and RP on
405 mitophagy (Fig. 6C). Remarkably, CQ treatment over 6 weeks in the patient fibroblasts and cybrid cells
406 also prevented the decrease of mutant load by PI3K-Akt-mTORC1 inhibition (Fig. 6D-E), strongly

407 suggesting that increased mitophagy is necessary to reduce the burden of mutant mtDNA. This also
408 argues strongly that the reduction in mutant load must be a cell-autonomous effect and cannot be
409 attributed to the selective growth of subpopulations of the cells. Together, effective
410 autophagy/mitophagy triggered by inhibition of the PI3K-Akt-mTORC1 axis is necessary to eliminate
411 the mutant m.3243A>G mtDNA.

412 **DISCUSSION**

413 The clinical presentation of disease caused by pathogenic mtDNA mutations is highly heterogeneous[4–
414 6]. The association between specific mtDNA mutations, heteroplasmic mutant load, disease
415 manifestation and severity are poorly understood. In the present study, we have systematically
416 characterised the metabolic and cell signalling phenotype of cells bearing the m.3243A>G mutation,
417 the most prevalent mtDNA mutation which is responsible for mitochondrial encephalomyopathy,
418 lactic acidosis and stroke-like episodes (MELAS) or Maternally inherited Diabetes and Deafness (MIDD)
419 and related disorders. We found that the changes in metabolism were associated with the constitutive
420 hyperactivation of the PI3K-Akt-mTORC1 pathway specifically associated with the m.3243A>G mtDNA
421 mutation. Most notably, pharmacological inhibition of PI3K, Akt, or mTORC1 in the patient-derived
422 cells reduced mutant load and rescued mitochondrial bioenergetic function. These inhibitors
423 promoted the upregulation of mitophagy, which was absolutely required to mediate the effects of
424 these treatments (Fig. 6F). In contrast to the m.3243A>G mtDNA variant, previous studies have
425 reported downregulation of Akt activity in cells carrying the m.8993T>G mutation[35], in which inhibition
426 of the PI3K-Akt-mTORC1 pathway had no impact on mutant load or mitochondrial function (Fig. S5J).
427 These findings suggest that the changes in signalling pathways are disease specific and may represent
428 a link between genotype and phenotype.

429 Metabolic features of the patient fibroblasts and cybrid cells are consistent with most of the previous
430 studies of the m.3243A>G mutation, including mitochondrial dysfunction, upregulated glycolysis,
431 increased ROS production, and redox imbalance[5,15,19,30,32,36]. However, metabolic profiling of cells
432 bearing the mutation is limited in the literature. Metabolomics data showed that reductive
433 carboxylation of glutamine is a major mechanism to support cell survival and maintain redox balance
434 in the m.8993T>G mutation cell models[27,37]. In contrast, using a similar approach, we found that
435 glucose anabolism (i.e. upregulated upper glycolysis, PPP, and lipid synthesis) is increased in the
436 m.3243A>G mutant cells and these cells are dependent on glucose for cell survival and proliferation.
437 Also, increased TCA cycle entry of pyruvate through PC, which, combined with the prediction of
438 enriched malate-aspartate shuttle pathway (Fig. 2A) may serve as a mechanism to maintain cellular
439 $NADH/NAD^+$ balance to support glycolytic flux and promote antioxidant capacity[27,38]. This difference
440 in metabolism between the m.8993T>G and m.3243A>G mutations argues that the mtDNA mutations
441 cannot be seen as one disease[29,39]. Thus, the rewired metabolism specific to the m.3243A>G mutation
442 drew our attention to the corresponding changes in cell signalling.

443 The alterations of metabolism in the m.3243A>G mutant cells strongly imply a perturbation in cell
444 signalling, especially implicating the PI3K-Akt-mTORC1 pathway, which has been widely studied in

445 cancer signalling and metabolism[40]. For example, oxidative stress and redox imbalance may activate
446 PI3K-Akt, the increased glycolytic flux and PPP implies an activated Akt-NRF2 signalling, the increased
447 PC expression and p-PDH suggests an accumulation of acetyl-CoA associated with Akt-mTORC1
448 activity, and the accumulation of cholesteryl ester can result from excessive lysosomal free
449 cholesterol, which also activates mTORC1[40,41]. Metabolic pathway analysis using RNA-seq data
450 recapitulated these metabolic changes in the patient fibroblasts. Moreover, network analysis using
451 the RNA-seq data further validated the link between the metabolic changes and altered cell signalling
452 in cells carrying the m.3243A>G mutation. In addition, defective autophagy, because of chronic
453 activation of the PI3K-Akt-mTORC1 pathway, may impair the selective degradation of lipid droplets
454 (lipophagy) and contribute to the accumulation of lipid droplets in the m.3243A>G mutant cells.
455 Sphingomyelin accumulation, as one of the features of the lipidomic data, may damage lysosomes,
456 also contributing to impaired autophagy[13,42].

457 Although the mechanisms of crosstalk between PI3K-Akt-mTORC1 and EIF2 pathways are still unclear,
458 these two pathways seem to communicate and determine cell fate under stress[23,31]. Of note, the
459 ISR/UPR^{mt} mediated by the EIF2 signalling was also downregulated by pharmacological inhibition of
460 the PI3K-Akt-mTORC1 axis in the mutant cells. Given that the UPR^{mt} maintains mutant mtDNA in a *C.*
461 *elegans* mtDNA disease model[43] and recent studies reported that OMA1 is responsible for eIF2α
462 phosphorylation under acute mitochondrial stress[44,45], exploring the role of ISR/UPR^{mt} in the
463 maintenance of the m.3243A>G mutation and disease progression by suppressing eIF2α
464 phosphorylation will be interesting. Furthermore, in a published RNA-seq data set of muscle biopsies
465 from patients with MELAS[26], FGF21 (~48 fold) and GDF15 (~9 fold) were upregulated, matching
466 previous findings reported from muscle tissue of 'Deletor' mice[46]. In contrast, in the present study,
467 while we did not find changes in these two genes in the patient fibroblasts, we did find upregulation
468 of FGF16 (~33 fold), suggesting that changes in FGF pathways in response to mitochondrial dysfunction
469 might be tissue specific.

470 Previous studies have suggested that different levels of heteroplasmy of the m.3243A>G mutation in
471 cybrid cells result in different gene expression patterns and even in discrete changes in
472 metabolism[47,48]. Another study showed that JNK was activated by ROS in cybrid m.3243A>G cells,
473 further reducing RXRA expression[49]. In contrast, our data did not show inhibition of the RXRA pathway
474 and suggest that chronic activation of the PI3K-Akt-mTORC1 pathway is a general response in cells
475 with the m.3243A>G mutation despite very different levels of mutant load. Remarkably, we found that
476 prolonged treatment with inhibitors of each component of the PI3K-Akt-mTORC1 axis reliably and
477 reproducibly reduced mutant burden and rescued mitochondrial function in the mutant cells.
478 Although inhibition of the PI3K-Akt-mTORC1 axis has been shown to be beneficial in several

479 mitochondrial and neurological disease models, the underlying mechanisms remain elusive[13,21,50–52].
480 As a result, the therapeutic efficacy of the inhibition may be distinct and limited in different models.
481 A study of a mouse model of Leigh syndrome showed that rapamycin, while delaying the progression
482 of the disease, failed to improve OxPhos[53]. Similarly, another study showed that mTORC1 inhibition
483 failed to improve either mitochondrial bioenergetics or survival in a mouse model of mitochondrial
484 encephalomyopathy ($Coq9^{R239X}$)[54]. Our data from cells with the m.8993T>G mutation suggest that
485 changes in signalling pathways may differ between mtDNA diseases, perhaps pointing towards the
486 mechanisms that define differences in disease phenotype between different mitochondrial diseases,
487 and emphasising that therapeutic options should be considered separately for each disease related to
488 mtDNA mutations. However, since both the PI3K-Akt-mTORC1 axis and the accumulation of mtDNA
489 mutations have been associated with neurodegeneration, ageing and cancers, our study may
490 implicate in a broader biomedical context[4,6,10,21,40].

491 Overall, the m.3243A>G mutation causes a profound cell metabolic and signalling remodelling,
492 although the causality between the observed alterations in metabolism and cell signalling of the
493 m.3243A>G mutant cells is not yet conclusive. Our working model is that activation of the PI3K-Akt-
494 mTORC1 pathway drives a metabolic rewiring of the cell, redirecting glycolytic metabolism and
495 promoting lactate production. Activating mTORC1 suppresses mitophagy, allowing the mutation to
496 propagate and thus maintaining the mutant load. Inhibition of the PI3K-Akt-mTORC1 axis promotes
497 mitophagy, reduces mutant load and improves bioenergetic competence in a cell-autonomous way.
498 Thus, we propose that nutrient-sensing pathways that may have evolved as adaptive responses to
499 altered cellular metabolism prove to be maladaptive, driving a positive feedback cycle that may shape
500 the phenotype of the disease and determine disease progression. In conclusion, our results suggest
501 that activation of the PI3K-Akt-mTORC1 axis by changes in intermediary metabolism controls the
502 heteroplasmic burden of the m.3243A>G mutation and may define disease progression and severity
503 in a cell-autonomous manner. These data strongly suggest that cell signalling pathways activated by
504 altered metabolism represent potential therapeutic targets that may benefit people suffering from
505 diseases caused by mtDNA mutations.

Figure 1

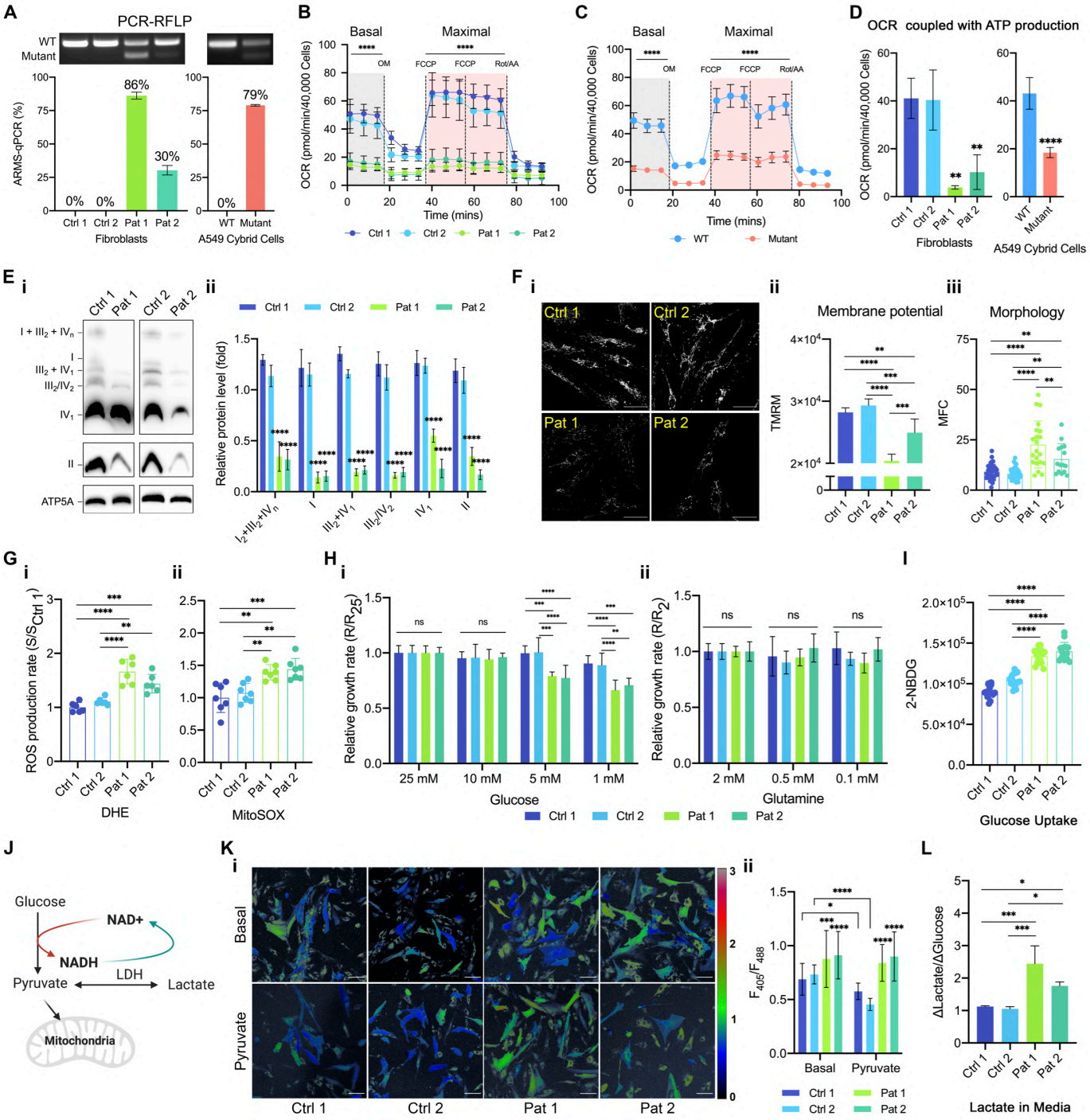
A
PCR-RFLP
WT
Mutant
ARMS-qPCR (%)
86%
30%
79%
0%
Ctrl 1
Ctrl 2
Pat 1
Pat 2
Fibroblasts
WT
Mutant
A549 Cybrid Cells
B
Basal
Maximal
OM
FCCP
Rot/AA
OCR (pmol/min/40,000 Cells)
Time (mins)
C
D
OCR coupled with ATP production
E
i
ii
Relative protein level (fold)
ATP5A
F
Membrane potential
Morphology
TMRM
MFC
G
ROS production rate (S/S$_{Ctrl 1}$)
DHE
MitoSOX
H
Relative growth rate (R/R$_{25}$)
Relative growth rate (R/R$_2$)
25 mM
10 mM
5 mM
1 mM
Glucose
2 mM
0.5 mM
0.1 mM
Glutamine
ns
I
2-NBDG
Glucose Uptake
J
Glucose
NAD+
NADH
LDH
Pyruvate
Lactate
Mitochondria
K
Basal
Pyruvate
F$_{405}$/F$_{488}$
L
ΔLactate/ΔGlucose
Lactate in Media

Figure S1

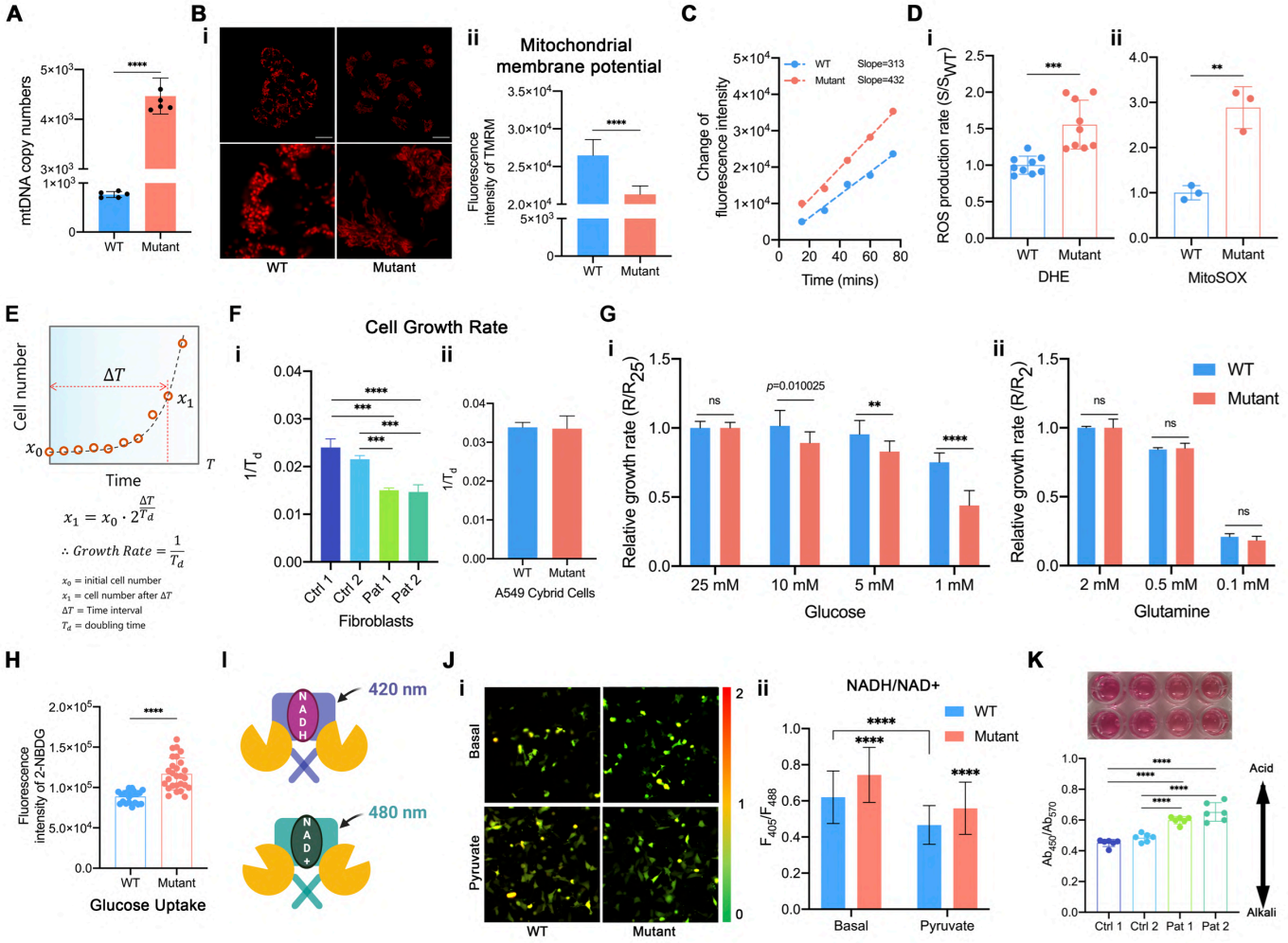
A
mtDNA copy numbers
WT
Mutant
B
i
WT
Mutant
ii
Mitochondrial membrane potential
Fluorescence intensity of TMRM
C
Change of fluorescence intensity
WT Slope=313
Mutant Slope=432
Time (mins)
D
i
ROS production rate (S/S_WT)
DHE
ii
MitoSOX
E
Cell number
Time
ΔT
x_1
x_0
T
x_1 = x_0 · 2^(ΔT/T_d)
∴ Growth Rate = 1/T_d
x_0 = initial cell number
x_1 = cell number after ΔT
ΔT = Time interval
T_d = doubling time
F
Cell Growth Rate
i
1/T_d
Ctrl 1
Ctrl 2
Pat 1
Pat 2
Fibroblasts
ii
A549 Cybrid Cells
G
i
Relative growth rate (R/R_25)
p=0.010025
25 mM
10 mM
5 mM
1 mM
Glucose
ii
Relative growth rate (R/R_2)
WT
Mutant
2 mM
0.5 mM
0.1 mM
Glutamine
H
Fluorescence intensity of 2-NBDG
Glucose Uptake
I
420 nm
480 nm
NADH
NAD+
J
i
Basal
Pyruvate
WT
Mutant
ii
NADH/NAD+
F_405/F_488
Basal
Pyruvate
K
Ab_450/Ab_570
Acid
Alkali
Ctrl 1
Ctrl 2
Pat 1
Pat 2

Figure 2

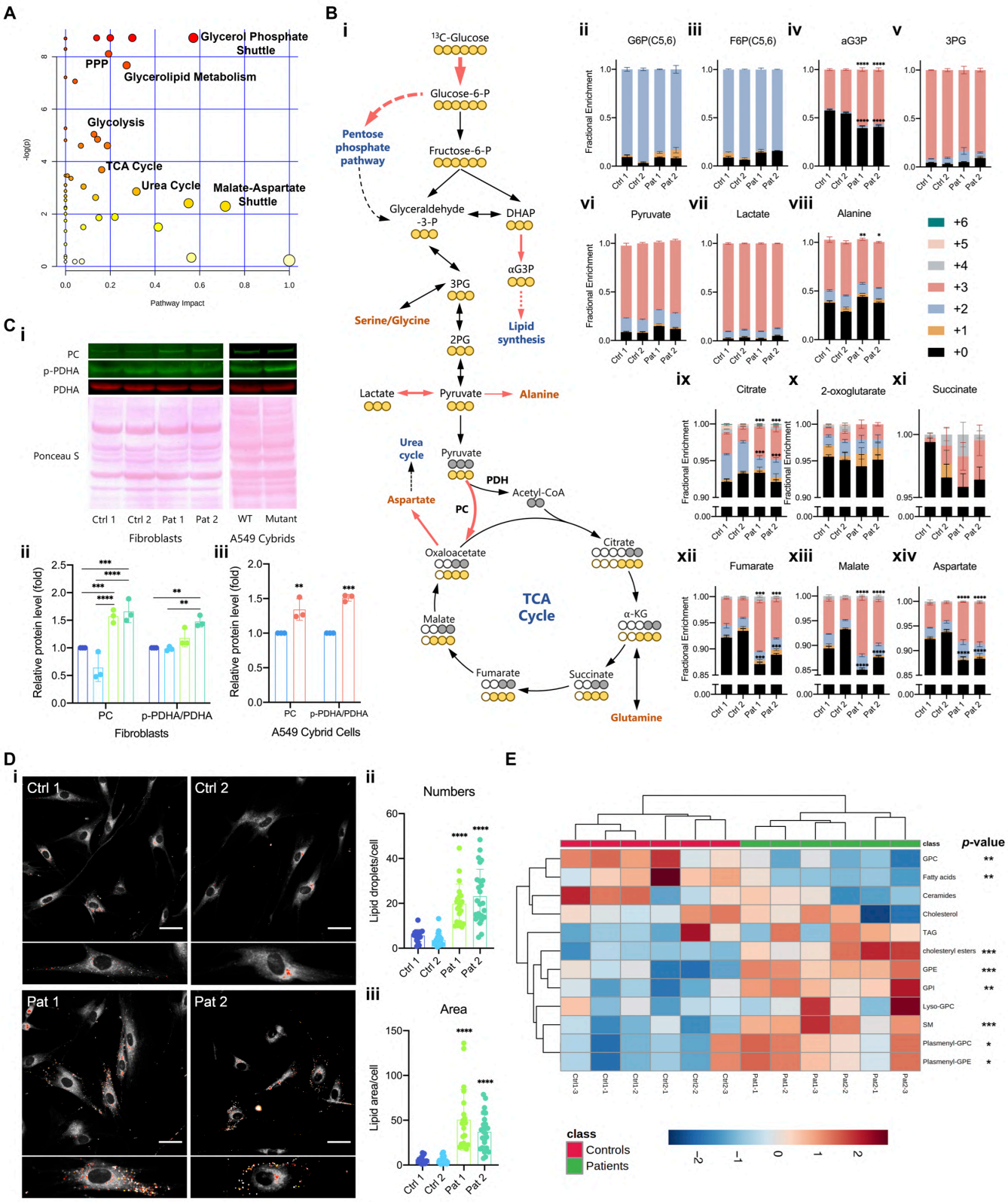
A
Glycerol Phosphate Shuttle
PPP
Glycerolipid Metabolism
Glycolysis
TCA Cycle
Urea Cycle
Malate-Aspartate Shuttle
-log(p)
Pathway Impact
B
i
13C-Glucose
Glucose-6-P
Pentose phosphate pathway
Fructose-6-P
Glyceraldehyde -3-P
DHAP
αG3P
3PG
Serine/Glycine
Lipid synthesis
2PG
Lactate
Pyruvate
Alanine
Urea cycle
Pyruvate
PDH
Acetyl-CoA
Aspartate
PC
Oxaloacetate
Citrate
TCA Cycle
Malate
α-KG
Fumarate
Succinate
Glutamine
ii G6P(C5,6)
iii F6P(C5,6)
iv aG3P
v 3PG
vi Pyruvate
vii Lactate
viii Alanine
ix Citrate
x 2-oxoglutarate
xi Succinate
xii Fumarate
xiii Malate
xiv Aspartate
Fractional Enrichment
Ctrl 1
Ctrl 2
Pat 1
Pat 2
+6
+5
+4
+3
+2
+1
+0
C
i
PC
p-PDHA
PDHA
Ponceau S
Ctrl 1
Ctrl 2
Pat 1
Pat 2
WT
Mutant
Fibroblasts
A549 Cybrids
ii
Relative protein level (fold)
PC
p-PDHA/PDHA
Fibroblasts
iii
Relative protein level (fold)
PC
p-PDHA/PDHA
A549 Cybrid Cells
D
i
Ctrl 1
Ctrl 2
Pat 1
Pat 2
ii
Numbers
Lipid droplets/cell
iii
Area
Lipid area/cell
E
class
p-value
GPC
Fatty acids
Ceramides
Cholesterol
TAG
cholesteryl esters
GPE
GPI
Lyso-GPC
SM
Plasmenyl-GPC
Plasmenyl-GPE
class
Controls
Patients

Figure S2

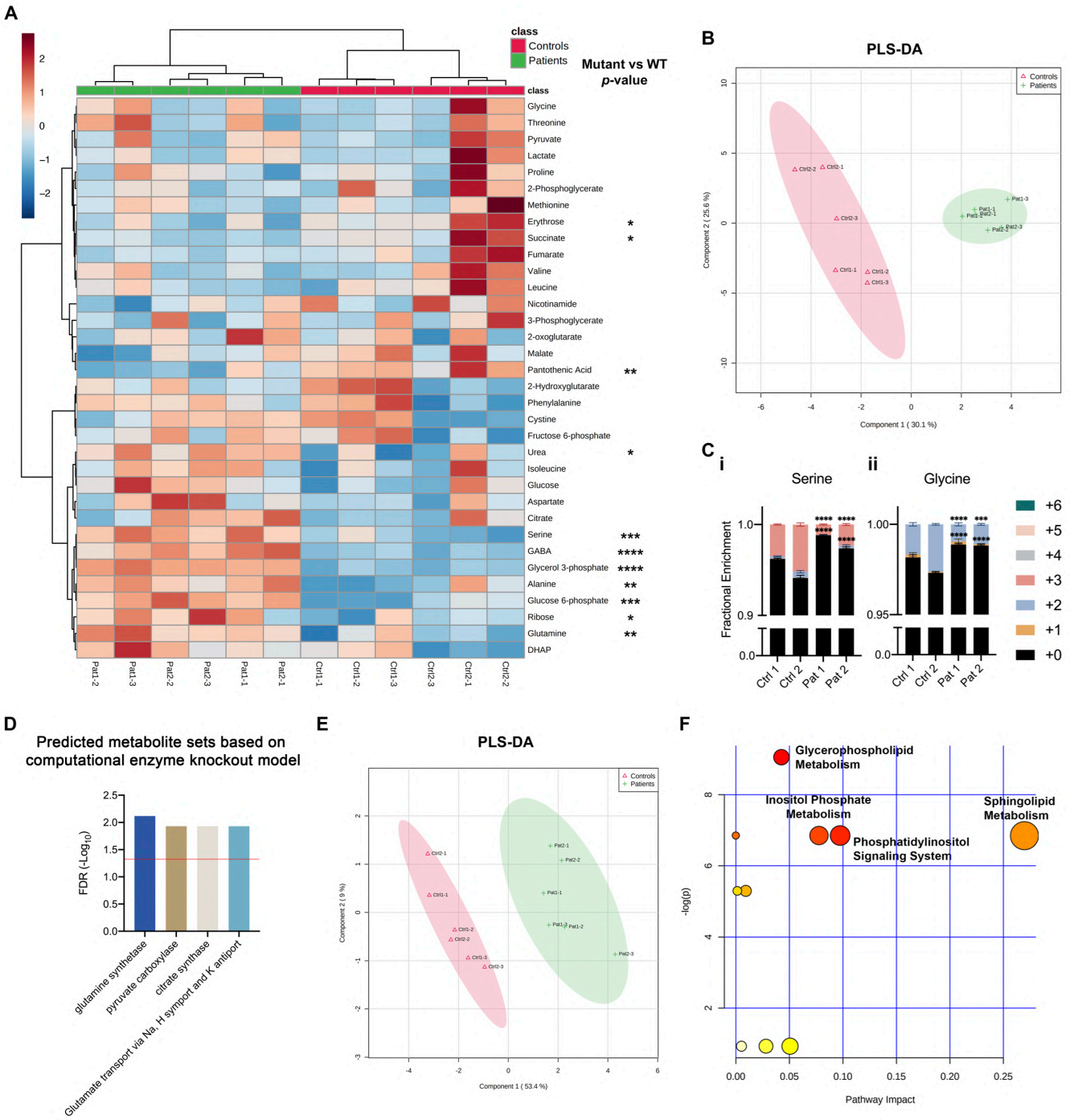
A
class
Controls
Patients
Mutant vs WT
p-value
Glycine
Threonine
Pyruvate
Lactate
Proline
2-Phosphoglycerate
Methionine
Erythrose *
Succinate *
Fumarate
Valine
Leucine
Nicotinamide
3-Phosphoglycerate
2-oxoglutarate
Malate
Pantothenic Acid **
2-Hydroxyglutarate
Phenylalanine
Cystine
Fructose 6-phosphate
Urea *
Isoleucine
Glucose
Aspartate
Citrate
Serine ***
GABA ****
Glycerol 3-phosphate ****
Alanine **
Glucose 6-phosphate ***
Ribose *
Glutamine **
DHAP
Pat1-2
Pat1-3
Pat2-2
Pat2-3
Pat1-1
Pat2-1
Ctrl1-1
Ctrl1-2
Ctrl1-3
Ctrl2-3
Ctrl2-1
Ctrl2-2
B
PLS-DA
Controls
Patients
Component 1 (30.1 %)
Component 2 (25.6 %)
C
i
Serine
ii
Glycine
Fractional Enrichment
Ctrl 1
Ctrl 2
Pat 1
Pat 2
+6
+5
+4
+3
+2
+1
+0
D
Predicted metabolite sets based on computational enzyme knockout model
FDR (-Log10)
glutamine synthetase
pyruvate carboxylase
citrate synthase
Glutamate transport via Na, H symport and K antiport
E
PLS-DA
Controls
Patients
Component 1 (53.4 %)
Component 2 (9 %)
F
Glycerophospholipid Metabolism
Inositol Phosphate Metabolism
Sphingolipid Metabolism
Phosphatidylinositol Signaling System
-log(p)
Pathway Impact

Figure 3

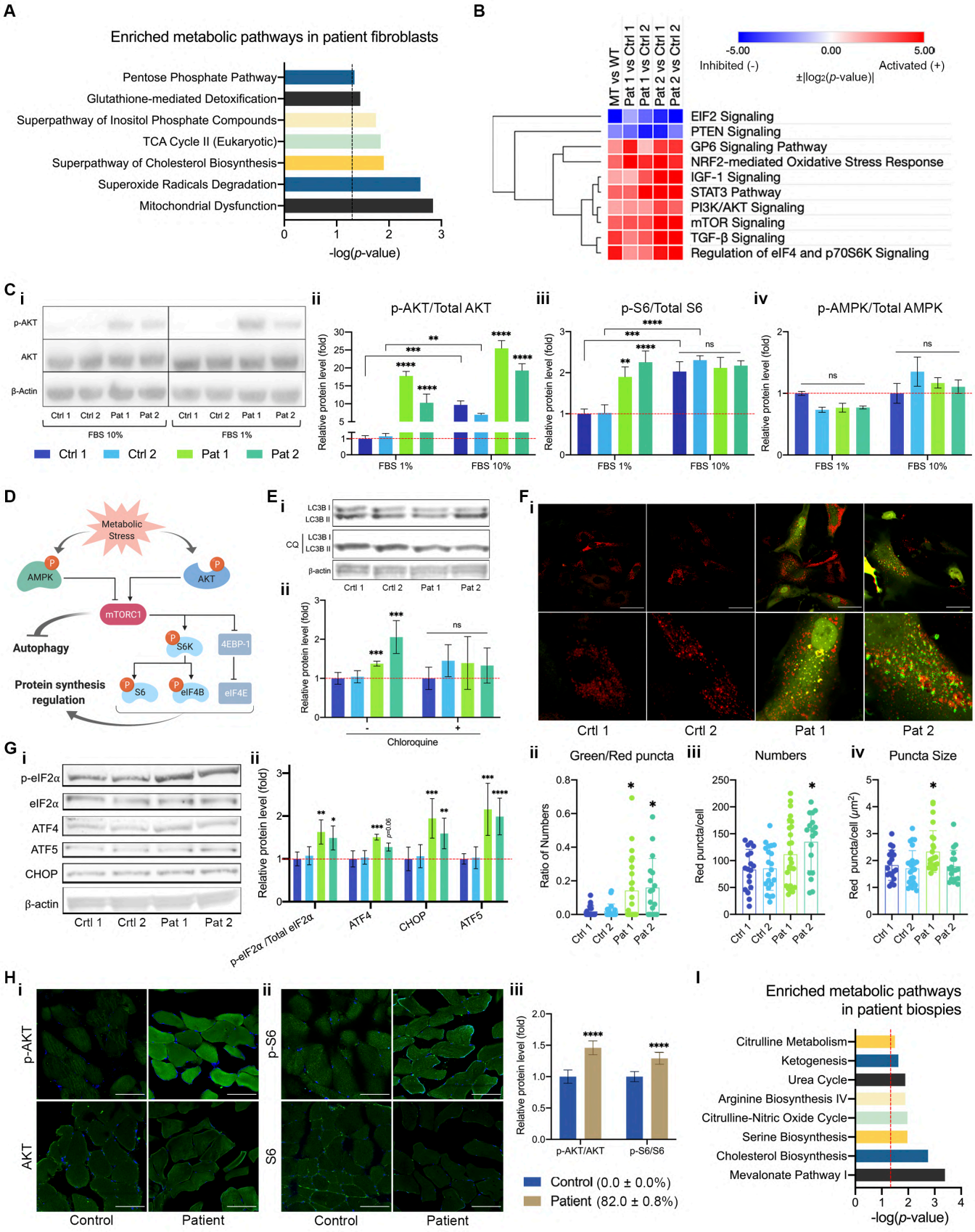
A
Enriched metabolic pathways in patient fibroblasts
Pentose Phosphate Pathway
Glutathione-mediated Detoxification
Superpathway of Inositol Phosphate Compounds
TCA Cycle II (Eukaryotic)
Superpathway of Cholesterol Biosynthesis
Superoxide Radicals Degradation
Mitochondrial Dysfunction
-log(p-value)
B
MT vs WT
Pat 1 vs Ctrl 1
Pat 1 vs Ctrl 2
Pat 2 vs Ctrl 1
Pat 2 vs Ctrl 2
-5.00
0.00
5.00
Inhibited (-)
Activated (+)
±|log2(p-value)|
EIF2 Signaling
PTEN Signaling
GP6 Signaling Pathway
NRF2-mediated Oxidative Stress Response
IGF-1 Signaling
STAT3 Pathway
PI3K/AKT Signaling
mTOR Signaling
TGF-β Signaling
Regulation of eIF4 and p70S6K Signaling
C
p-AKT
AKT
β-Actin
Ctrl 1
Ctrl 2
Pat 1
Pat 2
FBS 10%
FBS 1%
p-AKT/Total AKT
p-S6/Total S6
p-AMPK/Total AMPK
Relative protein level (fold)
ns
D
Metabolic Stress
AMPK
AKT
mTORC1
Autophagy
S6K
4EBP-1
Protein synthesis regulation
S6
eIF4B
eIF4E
E
LC3B I
LC3B II
CQ
β-actin
Chloroquine
F
Green/Red puncta
Numbers
Puncta Size
Ratio of Numbers
Red puncta/cell
Red puncta/cell (μm²)
G
p-eIF2α
eIF2α
ATF4
ATF5
CHOP
p-eIF2α /Total eIF2α
H
p-AKT
AKT
p-S6
S6
Control
Patient
p-AKT/AKT
p-S6/S6
Control (0.0 ± 0.0%)
Patient (82.0 ± 0.8%)
I
Enriched metabolic pathways in patient biospies
Citrulline Metabolism
Ketogenesis
Urea Cycle
Arginine Biosynthesis IV
Citrulline-Nitric Oxide Cycle
Serine Biosynthesis
Cholesterol Biosynthesis
Mevalonate Pathway I
-log(p-value)

Figure S3

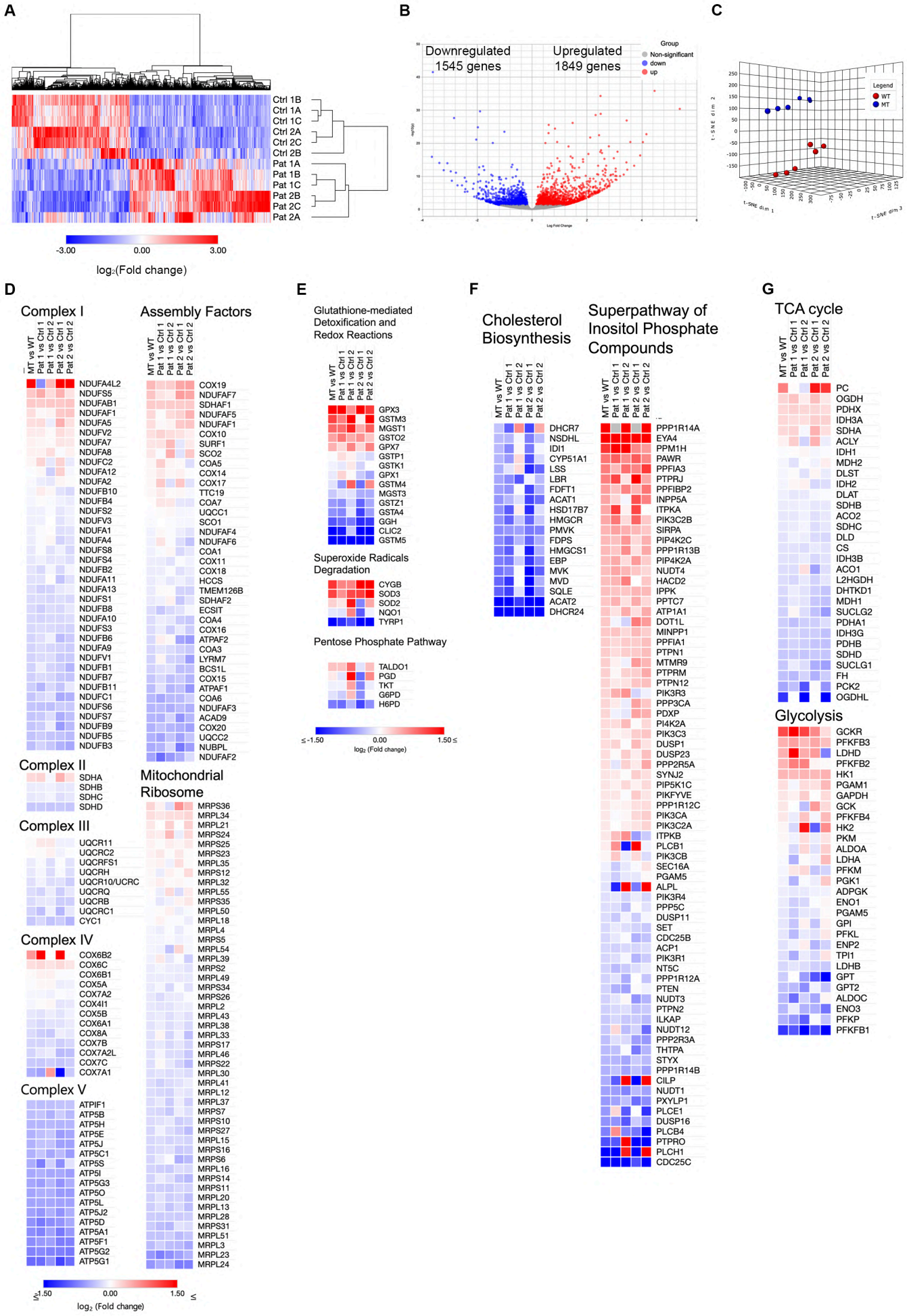
A
Ctrl 1B
Ctrl 1A
Ctrl 1C
Ctrl 2A
Ctrl 2C
Ctrl 2B
Pat 1A
Pat 1B
Pat 1C
Pat 2B
Pat 2C
Pat 2A
-3.00
0.00
3.00
log2(Fold change)
B
Downregulated
1545 genes
Upregulated
1849 genes
Group
Non-significant
down
up
Log Fold Change
C
Legend
WT
MT
t-SNE dim 1
t-SNE dim 2
t-SNE dim 3
D
Complex I
MT vs WT
Pat 1 vs Ctrl 1
Pat 1 vs Ctrl 2
Pat 2 vs Ctrl 1
Pat 2 vs Ctrl 2
NDUFA4L2
NDUFS5
NDUFAB1
NDUFAF1
NDUFA5
NDUFV2
NDUFA7
NDUFA8
NDUFC2
NDUFA12
NDUFA2
NDUFB10
NDUFB4
NDUFS2
NDUFV3
NDUFA1
NDUFA4
NDUFS8
NDUFS4
NDUFB2
NDUFA11
NDUFA13
NDUFS1
NDUFB8
NDUFA10
NDUFS3
NDUFB6
NDUFA9
NDUFV1
NDUFB1
NDUFB7
NDUFB11
NDUFC1
NDUFS6
NDUFS7
NDUFB9
NDUFB5
NDUFB3
Complex II
SDHA
SDHB
SDHC
SDHD
Complex III
UQCR11
UQCRC2
UQCRFS1
UQCRH
UQCR10/UCRC
UQCRQ
UQCRB
UQCRC1
CYC1
Complex IV
COX6B2
COX6C
COX6B1
COX5A
COX7A2
COX4I1
COX5B
COX6A1
COX8A
COX7B
COX7A2L
COX7C
COX7A1
Complex V
ATPIF1
ATP5B
ATP5H
ATP5E
ATP5J
ATP5C1
ATP5S
ATP5I
ATP5G3
ATP5O
ATP5L
ATP5J2
ATP5D
ATP5A1
ATP5F1
ATP5G2
ATP5G1
Assembly Factors
COX19
NDUFAF7
SDHAF1
NDUFAF5
NDUFAF1
COX10
SURF1
SCO2
COA5
COX14
COX17
TTC19
COA7
UQCC1
SCO1
NDUFAF4
NDUFAF6
COA1
COX11
COX18
HCCS
TMEM126B
SDHAF2
ECSIT
COA4
COX16
ATPAF2
COA3
LYRM7
BCS1L
COX15
ATPAF1
COA6
NDUFAF3
ACAD9
COX20
UQCC2
NUBPL
NDUFAF2
Mitochondrial Ribosome
MRPS36
MRPL34
MRPL21
MRPS24
MRPS25
MRPS23
MRPL35
MRPS12
MRPL32
MRPL55
MRPS35
MRPL50
MRPL18
MRPL4
MRPS5
MRPL54
MRPL39
MRPS2
MRPL49
MRPS34
MRPS26
MRPL2
MRPL43
MRPL38
MRPL33
MRPS17
MRPL46
MRPS22
MRPL30
MRPL41
MRPL12
MRPL37
MRPS7
MRPS10
MRPS27
MRPL15
MRPS16
MRPS6
MRPL16
MRPS14
MRPS11
MRPL20
MRPL13
MRPL28
MRPS31
MRPL51
MRPL3
MRPL23
MRPL24
≤-1.50
0.00
1.50 ≤
log2 (Fold change)
E
Glutathione-mediated Detoxification and Redox Reactions
MT vs WT
Pat 1 vs Ctrl 1
Pat 1 vs Ctrl 2
Pat 2 vs Ctrl 1
Pat 2 vs Ctrl 2
GPX3
GSTM3
MGST1
GSTO2
GPX7
GSTP1
GSTK1
GPX1
GSTM4
MGST3
GSTZ1
GSTA4
GGH
CLIC2
GSTM5
Superoxide Radicals Degradation
CYGB
SOD3
SOD2
NQO1
TYRP1
Pentose Phosphate Pathway
TALDO1
PGD
TKT
G6PD
H6PD
≤-1.50
0.00
1.50 ≤
log2 (Fold change)
F
Cholesterol Biosynthesis
MT vs WT
Pat 1 vs Ctrl 1
Pat 1 vs Ctrl 2
Pat 2 vs Ctrl 1
Pat 2 vs Ctrl 2
DHCR7
NSDHL
IDI1
CYP51A1
LSS
LBR
FDFT1
ACAT1
HSD17B7
HMGCR
PMVK
FDPS
HMGCS1
EBP
MVK
MVD
SQLE
ACAT2
DHCR24
Superpathway of Inositol Phosphate Compounds
MT vs WT
Pat 1 vs Ctrl 1
Pat 1 vs Ctrl 2
Pat 2 vs Ctrl 1
Pat 2 vs Ctrl 2
PPP1R14A
EYA4
PPM1H
PAWR
PPFIA3
PTPRJ
PPFIBP2
INPP5A
ITPKA
PIK3C2B
SIRPA
PIP4K2C
PPP1R13B
PIP4K2A
NUDT4
HACD2
IPPK
PPTC7
ATP1A1
DOT1L
MINPP1
PPFIA1
PTPN1
MTMR9
PTPRM
PTPN12
PIK3R3
PPP3CA
PDXP
PI4K2A
PIK3C3
DUSP1
DUSP23
PPP2R5A
SYNJ2
PIP5K1C
PIKFYVE
PPP1R12C
PIK3CA
PIK3C2A
ITPKB
PLCB1
PIK3CB
SEC16A
PGAM5
ALPL
PIK3R4
PPP5C
DUSP11
SET
CDC25B
ACP1
PIK3R1
NT5C
PPP1R12A
PTEN
NUDT3
PTPN2
ILKAP
NUDT12
PPP2R3A
THTPA
STYX
PPP1R14B
CILP
NUDT1
PXYLP1
PLCE1
DUSP16
PLCB4
PTPRO
PLCH1
CDC25C
G
TCA cycle
MT vs WT
Pat 1 vs Ctrl 1
Pat 1 vs Ctrl 2
Pat 2 vs Ctrl 1
Pat 2 vs Ctrl 2
PC
OGDH
PDHX
IDH3A
SDHA
ACLY
IDH1
MDH2
DLST
IDH2
DLAT
SDHB
ACO2
SDHC
DLD
CS
IDH3B
ACO1
L2HGDH
DHTKD1
MDH1
SUCLG2
PDHA1
IDH3G
PDHB
SDHD
SUCLG1
FH
PCK2
OGDHL
Glycolysis
GCKR
PFKFB3
LDHD
PFKFB2
HK1
PGAM1
GAPDH
GCK
PFKFB4
HK2
PKM
ALDOA
LDHA
PFKM
PGK1
ADPGK
ENO1
PGAM5
GPI
PFKL
ENP2
TPI1
LDHB
GPT
GPT2
ALDOC
ENO3
PFKP
PFKFB1

Figure S4

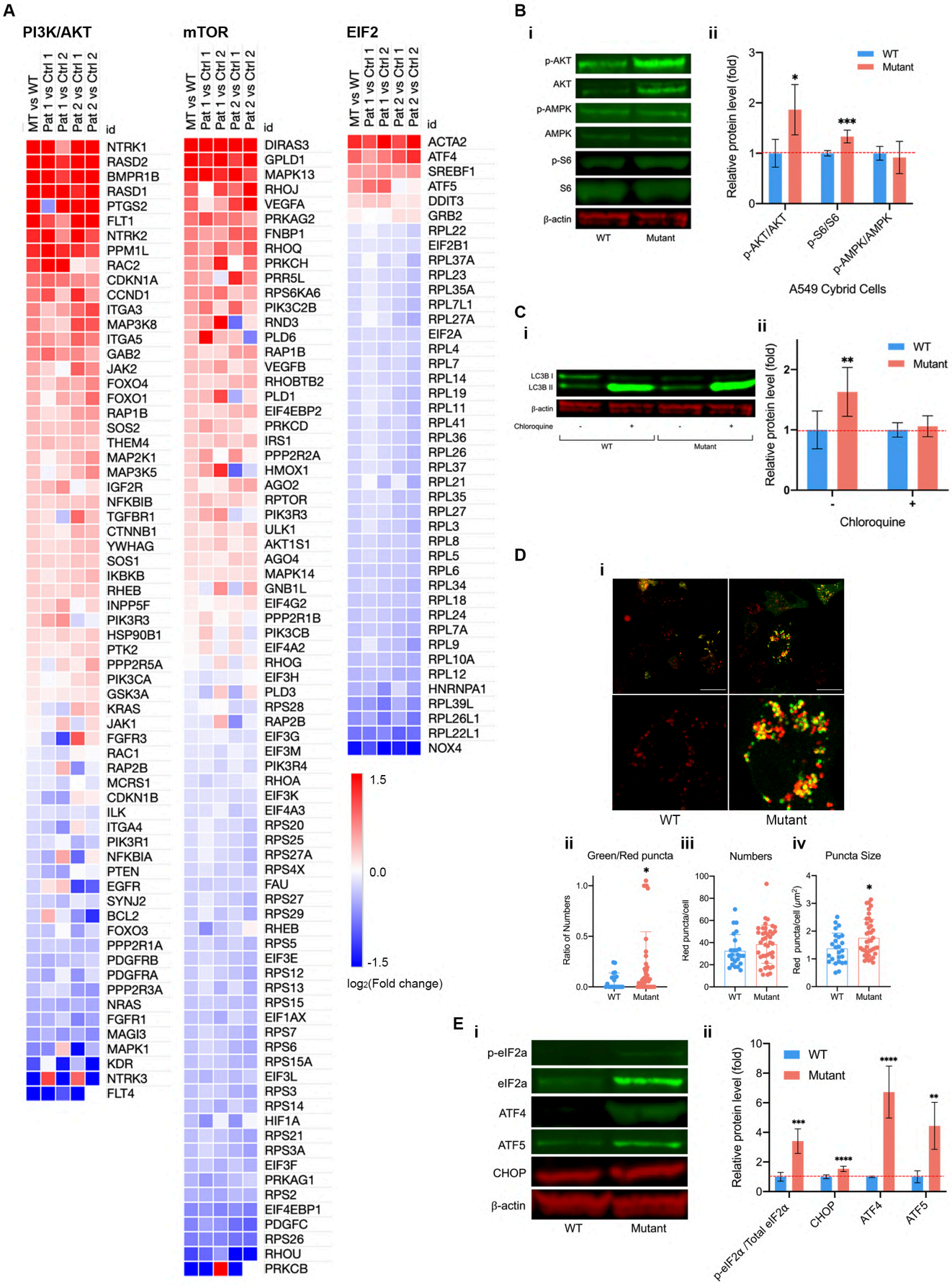
A
PI3K/AKT
mTOR
EIF2
MT vs WT
Pat 1 vs Ctrl 1
Pat 1 vs Ctrl 2
Pat 2 vs Ctrl 1
Pat 2 vs Ctrl 2
id
NTRK1
RASD2
BMPR1B
RASD1
PTGS2
FLT1
NTRK2
PPM1L
RAC2
CDKN1A
CCND1
ITGA3
MAP3K8
ITGA5
GAB2
JAK2
FOXO4
FOXO1
RAP1B
SOS2
THEM4
MAP2K1
MAP3K5
IGF2R
NFKBIB
TGFBR1
CTNNB1
YWHAG
SOS1
IKBKB
RHEB
INPP5F
PIK3R3
HSP90B1
PTK2
PPP2R5A
PIK3CA
GSK3A
KRAS
JAK1
FGFR3
RAC1
RAP2B
MCRS1
CDKN1B
ILK
ITGA4
PIK3R1
NFKBIA
PTEN
EGFR
SYNJ2
BCL2
FOXO3
PPP2R1A
PDGFRB
PDGFRA
PPP2R3A
NRAS
FGFR1
MAGI3
MAPK1
KDR
NTRK3
FLT4
DIRAS3
GPLD1
MAPK13
RHOJ
VEGFA
PRKAG2
FNBP1
RHOQ
PRKCH
PRR5L
RPS6KA6
PIK3C2B
RND3
PLD6
RAP1B
VEGFB
RHOBTB2
PLD1
EIF4EBP2
PRKCD
IRS1
PPP2R2A
HMOX1
AGO2
RPTOR
PIK3R3
ULK1
AKT1S1
AGO4
MAPK14
GNB1L
EIF4G2
PPP2R1B
PIK3CB
EIF4A2
RHOG
EIF3H
PLD3
RPS28
RAP2B
EIF3G
EIF3M
PIK3R4
RHOA
EIF3K
EIF4A3
RPS20
RPS25
RPS27A
RPS4X
FAU
RPS27
RPS29
RHEB
RPS5
EIF3E
RPS12
RPS13
RPS15
EIF1AX
RPS7
RPS6
RPS15A
EIF3L
RPS3
RPS14
HIF1A
RPS21
RPS3A
EIF3F
PRKAG1
RPS2
EIF4EBP1
PDGFC
RPS26
RHOU
PRKCB
ACTA2
ATF4
SREBF1
ATF5
DDIT3
GRB2
RPL22
EIF2B1
RPL37A
RPL23
RPL35A
RPL7L1
RPL27A
EIF2A
RPL4
RPL7
RPL14
RPL19
RPL11
RPL41
RPL36
RPL26
RPL37
RPL21
RPL35
RPL27
RPL3
RPL8
RPL5
RPL6
RPL34
RPL18
RPL24
RPL7A
RPL9
RPL10A
RPL12
HNRNPA1
RPL39L
RPL26L1
RPL22L1
NOX4
1.5
0.0
-1.5
log2(Fold change)
B
i
p-AKT
AKT
p-AMPK
AMPK
p-S6
S6
β-actin
WT
Mutant
ii
WT
Mutant
Relative protein level (fold)
p-AKT/AKT
p-S6/S6
p-AMPK/AMPK
A549 Cybrid Cells
C
i
LC3B I
LC3B II
β-actin
Chloroquine
WT
Mutant
ii
WT
Mutant
Relative protein level (fold)
Chloroquine
D
i
WT
Mutant
ii
Green/Red puncta
Ratio of Numbers
iii
Numbers
Red puncta/cell
iv
Puncta Size
Red puncta/cell (μm²)
E
i
p-eIF2a
eIF2a
ATF4
ATF5
CHOP
β-actin
WT
Mutant
ii
WT
Mutant
Relative protein level (fold)
p-eIF2α /Total eIF2α
CHOP
ATF4
ATF5

Table S1-4

Table S1. Upstream analysis for Kinase in patient fibroblasts by IPA.

Kinase	Prediction	Z-score	*p*-value
CDKN1A	Activated	3.084	1.12E-08
IKBKB		3.244	0.000377
AKT1		2.47	0.00201
MAPK13		2.079	0.00245
TGFBR2		2.747	0.00255
PTK2		2.48	0.00302
CHUK		4.427	0.00929
STK11	Inhibited	-2.494	0.00000766
INSR		-2.032	0.000675
CCNK		-2.399	0.000866
AURKB		-2.772	0.005

Table S2. Upstream analysis for translation regulator in patient fibroblasts by IPA.

Translation regulator	Prediction	Z-score	*p*-value
EIF4E	Inhibited	-2.169	0.000541
EIF4G1		-2.333	0.00245

Table S3. Upstream analysis for transcription regulators in patient fibroblasts by IPA.

Transcription regulator	Prediction	Z-score	*p*-value
TP53	Activated	3.282	2.79E-21
NUPR1		4.066	5.29E-11
KDM5B		3.627	0.00000101
CTNNB1		2.96	0.00000321
NFKBIA		2.632	0.0000157
GLI1		2.971	0.0000256
TCF4		2.225	0.0000457
SMARCA4		3.609	0.000108
KLF4		2.946	0.000627
PTTG1		2.302	0.000791
TFEB		3.273	0.0008
CDKN2A		4.62	0.000838
TCF7L2		4.059	0.000841
TCF3		3.926	0.00118
HIF1A		2.117	0.00224
CREB1		3.164	0.00238
HDAC1		2.228	0.00248
RBCK1		2.236	0.00252
E2F6		2.53	0.00259
ATF4		2.495	0.00296
SMARCD3		2.813	0.005
HDAC2		2.468	0.00621
ERG		2.557	0.00988
EP300		2.298	0.00994
TBX2	Inhibited	-4.488	2.43E-08
MYC		-4.01	2.46E-07
MYCN		-5.406	0.00000442
GMNN		-2.746	0.0000098
SOX1		-3	0.0000215
HOXA9		-2.01	0.0000273
E2F3		-3.186	0.0000273
SOX3		-3	0.00012
RUNX3		-2.272	0.000213

Table S4. Upstream analysis using published RNA-seq dataset of patient biopsies by IPA.

Upstream Regulator	Molecule Type	*p*-value
TRIB3	Kinase	0.0000295
MTOR		0.00112
TGFBR2		0.0101
GNE		0.0155
PIK3R1		0.0159
TGFBR1		0.0166
CDK19		0.0199
Growth hormone	Group	0.000165
Foxo		0.000504
ADRB		0.00393
Insulin		0.00402
YAP/TAZ		0.0089
Pro-inflammatory Cytokine		0.0101
PI3K (family)		0.026
Rxr		0.0269
ATF4	Transcription Regulator	0.00048
MLX		0.000905
PPARGC1A		0.00115
EP300		0.0029
FOXO1		0.00299
MLXIPL		0.00326
MLXIP		0.00446
ZNF282		0.0089
MYRF		0.0104
HDAC5		0.0122
NKX2-3		0.0127
MYC		0.0131
STAT6		0.0149
ZNF100		0.0155
ZNF85		0.0155
ZNF254		0.0155
ZNF431		0.0155
ZNF43		0.0155
ZNF429		0.0155
HDAC10		0.0177
ZNF91		0.0177
ATF5		0.0221
PA2G4		0.0221
KAT5		0.0231
STAT5B		0.026
AJUBA		0.0265
DDIT3		0.0282
BHLHE41		0.0287
ARNT		0.0304
PIAS4		0.0308
THRAP3		0.033
PLAGL1		0.033
KLF11		0.0337
CREBZF		0.0352
CBX4		0.0352
TCF7L2		0.0374
MNT		0.0416
ACTN4		0.0416
CREB3L3		0.0438
NONO		0.0438
MED12		0.0459
SIN3B		0.0459
PBX3		0.048
HNF4A		0.048
MED1		0.0492

Figure 4

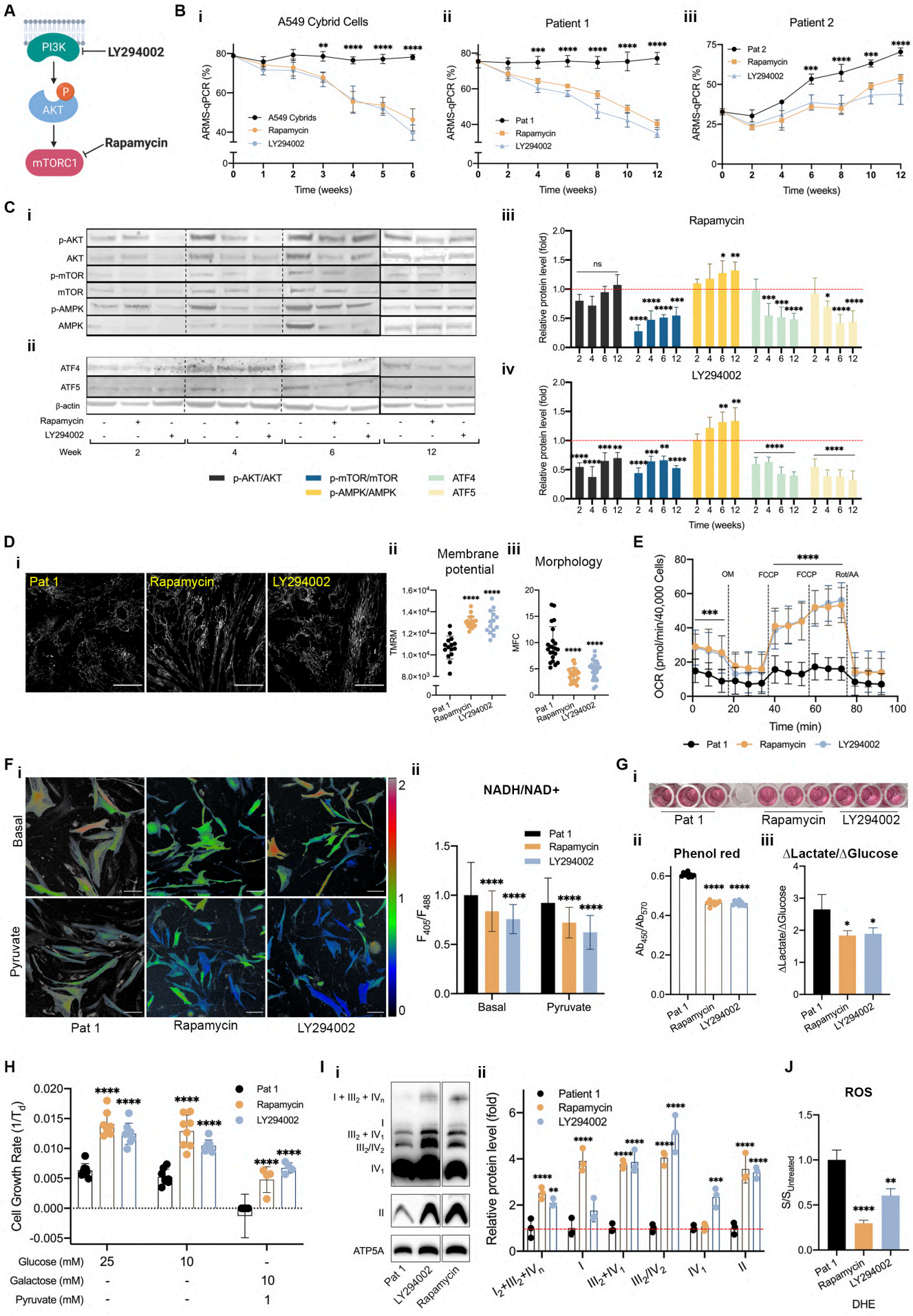
A
PI3K
LY294002
P
AKT
Rapamycin
mTORC1
B
i
A549 Cybrid Cells
ARMS-qPCR (%)
A549 Cybrids
Rapamycin
LY294002
Time (weeks)
ii
Patient 1
Pat 1
iii
Patient 2
Pat 2
C
i
p-AKT
AKT
p-mTOR
mTOR
p-AMPK
AMPK
ii
ATF4
ATF5
β-actin
Rapamycin
LY294002
Week
p-AKT/AKT
p-mTOR/mTOR
p-AMPK/AMPK
ATF4
ATF5
iii
Rapamycin
Relative protein level (fold)
iv
LY294002
Time (weeks)
D
i
Pat 1
Rapamycin
LY294002
ii
Membrane potential
TMRM
iii
Morphology
MFC
E
OCR (pmol/min/40,000 Cells)
OM
FCCP
FCCP
Rot/AA
Time (min)
F
i
Basal
Pyruvate
Pat 1
Rapamycin
LY294002
ii
NADH/NAD+
F_{405}/F_{488}
G
i
Pat 1
Rapamycin
LY294002
ii
Phenol red
Ab_{450}/Ab_{570}
iii
ΔLactate/ΔGlucose
H
Cell Growth Rate ($1/T_d$)
Glucose (mM)
Galactose (mM)
Pyruvate (mM)
I
i
$I + III_2 + IV_n$
I
$III_2 + IV_1$
III_2/IV_2
IV_1
II
ATP5A
ii
Relative protein level (fold)
$I_2+III_2+IV_n$
III_2+IV_1
III_2/IV_2
IV_1
J
ROS
$S/S_{Untreated}$
DHE

Figure S5

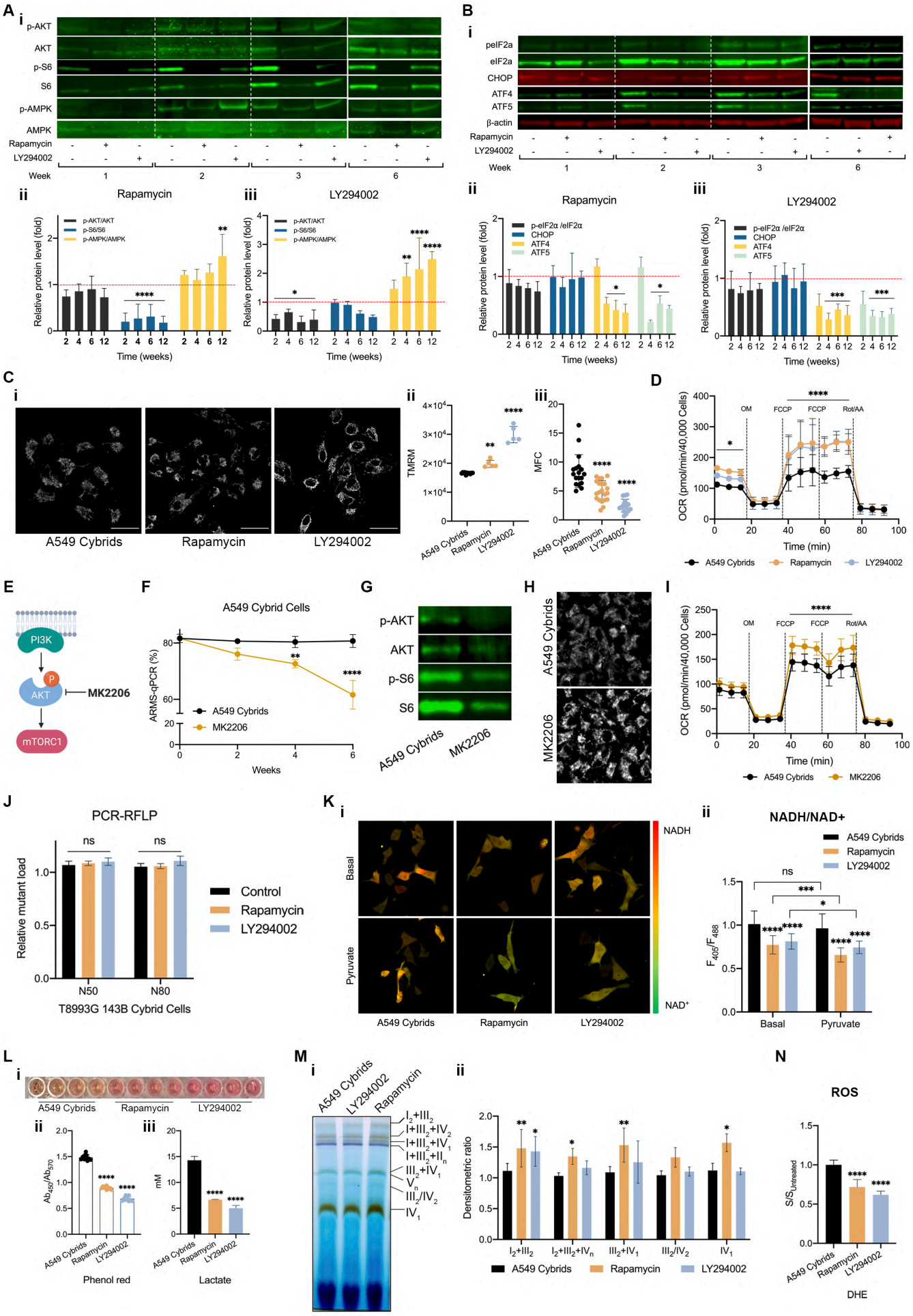
A
i
p-AKT
AKT
p-S6
S6
p-AMPK
AMPK
Rapamycin
LY294002
Week
1
2
3
6
ii
Rapamycin
iii
LY294002
p-AKT/AKT
p-S6/S6
p-AMPK/AMPK
Relative protein level (fold)
Time (weeks)
B
i
peIF2a
eIF2a
CHOP
ATF4
ATF5
β-actin
p-eIF2α /eIF2α
C
A549 Cybrids
Rapamycin
LY294002
TMRM
MFC
D
OCR (pmol/min/40,000 Cells)
OM
FCCP
Rot/AA
Time (min)
E
PI3K
AKT
mTORC1
MK2206
F
A549 Cybrid Cells
ARMS-qPCR (%)
Weeks
MK2206
G
p-AKT
AKT
p-S6
S6
H
I
J
PCR-RFLP
Relative mutant load
Control
N50
N80
T8993G 143B Cybrid Cells
K
NADH
NAD+
Basal
Pyruvate
NADH/NAD+
L
Phenol red
Lactate
M
I2+III2
I+III2+IV2
I+III2+IV1
I+III2+IIn
III2+IV1
Vn
III2/IV2
IV1
Densitometric ratio
N
ROS
DHE

Figure 5

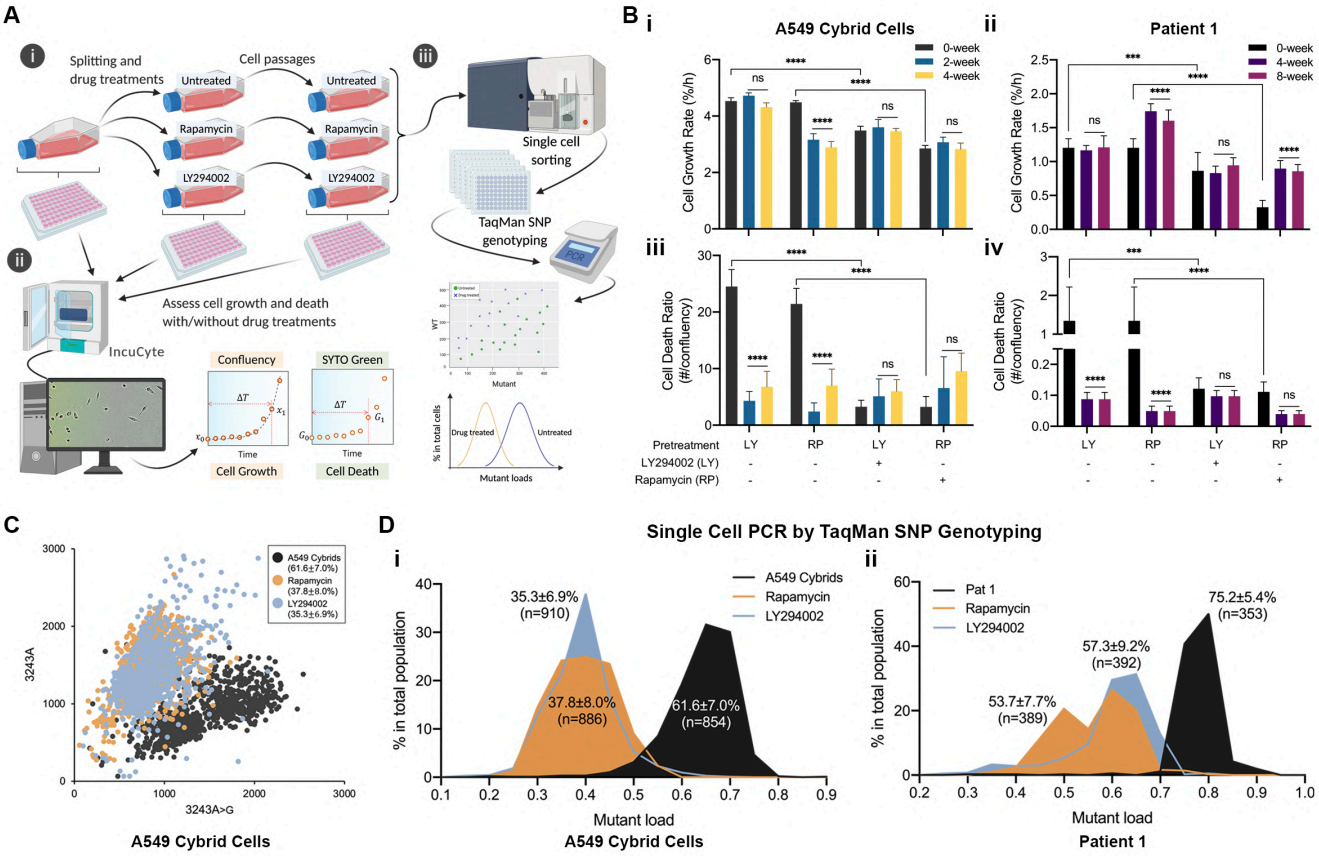
A
i
Splitting and drug treatments
Cell passages
Untreated
Rapamycin
LY294002
ii
Assess cell growth and death with/without drug treatments
IncuCyte
Confluency
SYTO Green
Time
Cell Growth
Cell Death
iii
Single cell sorting
TaqMan SNP genotyping
PCR
Mutant
Mutant loads
Drug treated
Untreated
B
i
A549 Cybrid Cells
ii
Patient 1
0-week
2-week
4-week
8-week
Cell Growth Rate (%/h)
iii
iv
Cell Death Ratio (#/confluency)
Pretreatment
LY294002 (LY)
Rapamycin (RP)
LY
RP
C
A549 Cybrids (61.6±7.0%)
Rapamycin (37.8±8.0%)
LY294002 (35.3±6.9%)
3243A
3243A>G
A549 Cybrid Cells
D
Single Cell PCR by TaqMan SNP Genotyping
i
A549 Cybrids
Rapamycin
LY294002
35.3±6.9% (n=910)
37.8±8.0% (n=886)
61.6±7.0% (n=854)
% in total population
Mutant load
A549 Cybrid Cells
ii
Pat 1
Rapamycin
LY294002
53.7±7.7% (n=389)
57.3±9.2% (n=392)
75.2±5.4% (n=353)
Patient 1

Figure S6

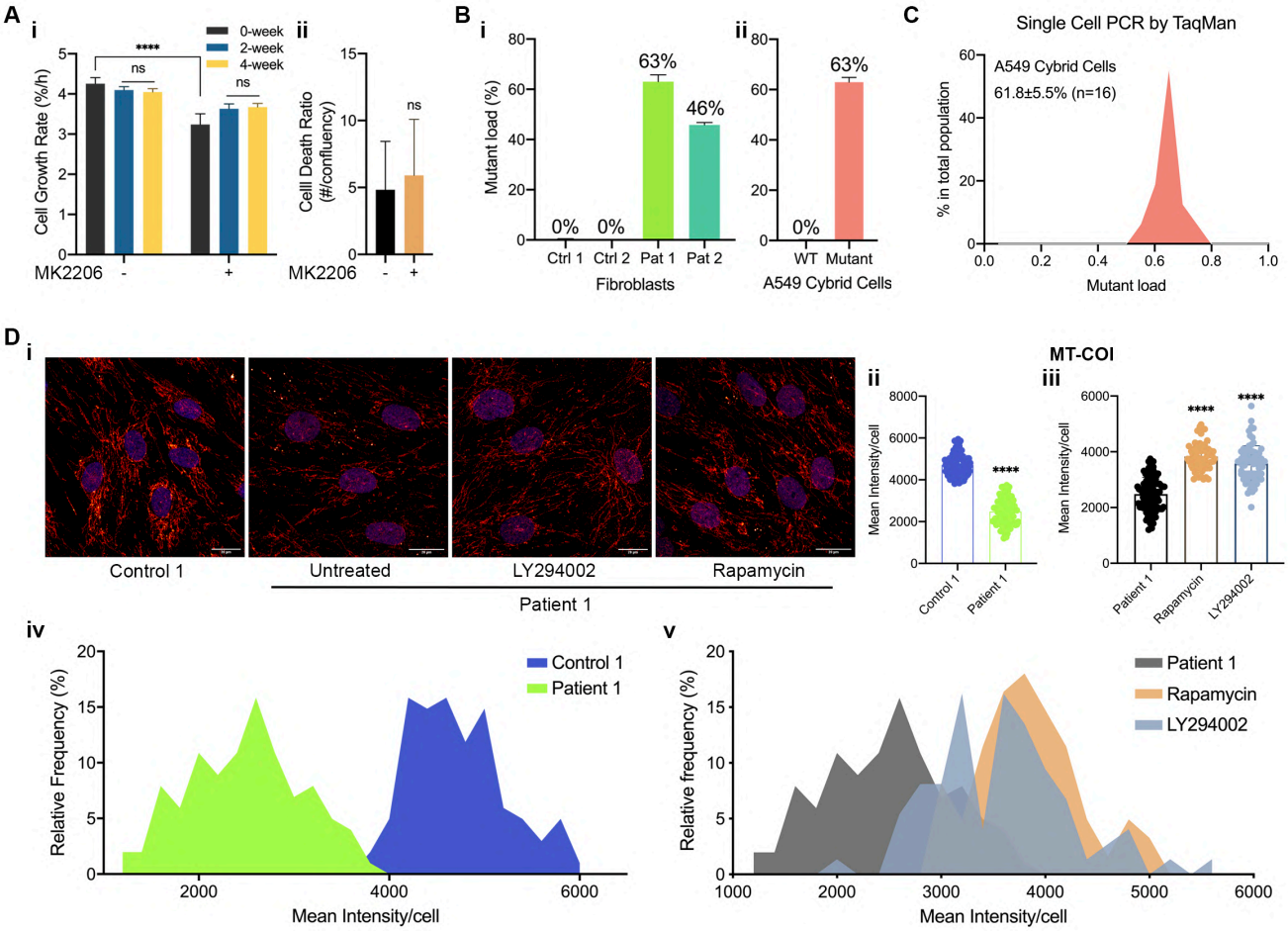
A
i
0-week
2-week
4-week
****
ns
ns
Cell Growth Rate (%/h)
MK2206
-
+
ii
Celll Death Ratio (#/confluency)
ns
MK2206
-
+
B
i
Mutant load (%)
0%
0%
63%
46%
Ctrl 1
Ctrl 2
Pat 1
Pat 2
Fibroblasts
ii
0%
63%
WT
Mutant
A549 Cybrid Cells
C
Single Cell PCR by TaqMan
A549 Cybrid Cells
61.8±5.5% (n=16)
% in total population
Mutant load
D
i
Control 1
Untreated
LY294002
Rapamycin
Patient 1
ii
Mean Intensity/cell
****
Control 1
Patient 1
MT-COI
iii
Mean Intensity/cell
****
****
Patient 1
Rapamycin
LY294002
iv
Relative Frequency (%)
Control 1
Patient 1
Mean Intensity/cell
v
Relative frequency (%)
Patient 1
Rapamycin
LY294002
Mean Intensity/cell

Figure 6

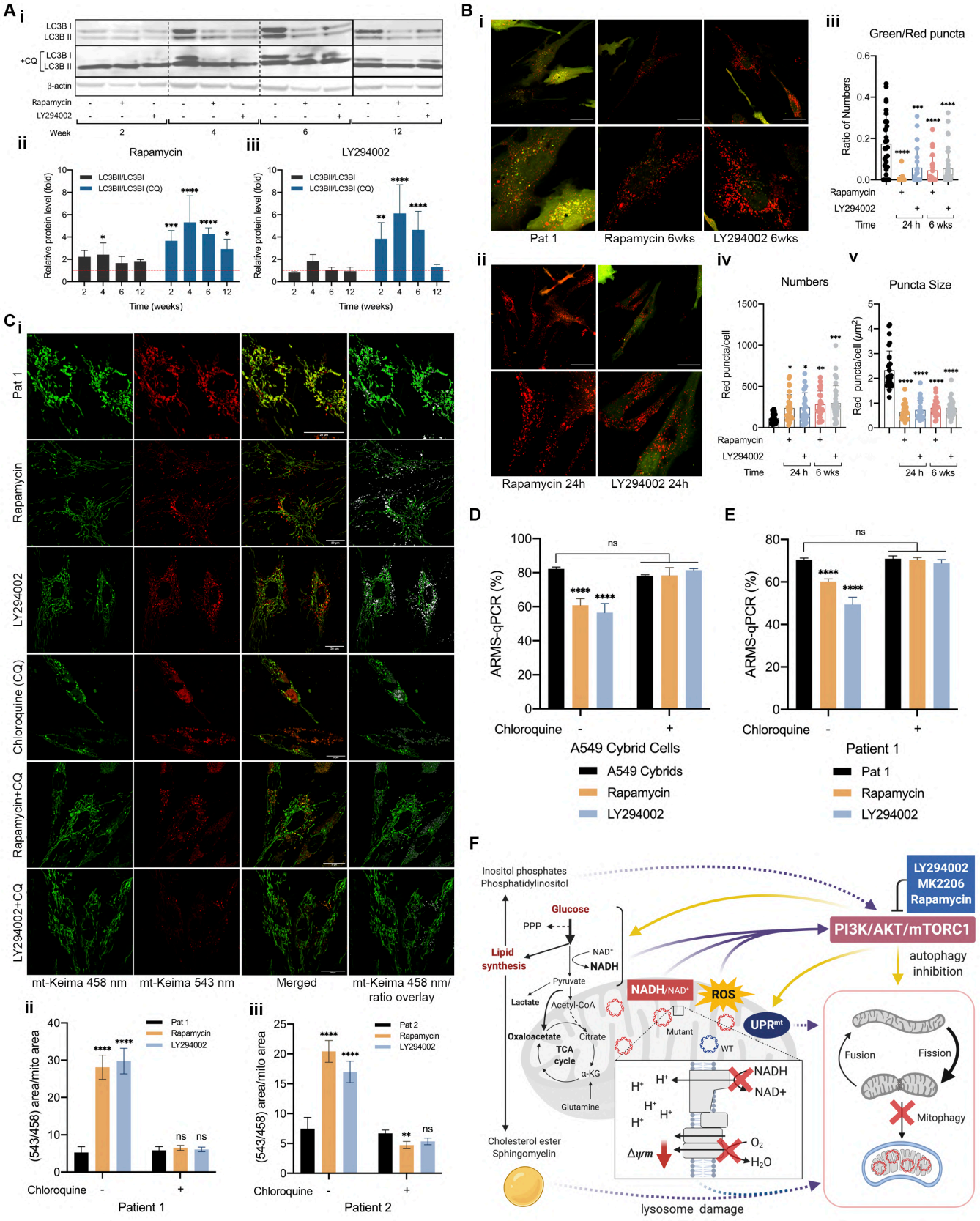
A
i
LC3B I
LC3B II
+CQ
β-actin
Rapamycin
LY294002
Week
ii
Rapamycin
iii
LY294002
LC3BII/LC3BI
LC3BII/LC3BI (CQ)
Relative protein level (fold)
Time (weeks)
B
i
Pat 1
Rapamycin 6wks
LY294002 6wks
ii
Rapamycin 24h
LY294002 24h
iii
Green/Red puncta
Ratio of Numbers
iv
Numbers
Red puncta/cell
v
Puncta Size
Red puncta/cell (μm²)
Time
24 h
6 wks
C
i
Pat 1
Rapamycin
LY294002
Chloroquine (CQ)
Rapamycin+CQ
LY294002+CQ
mt-Keima 458 nm
mt-Keima 543 nm
Merged
mt-Keima 458 nm/ ratio overlay
ii
Pat 1
Rapamycin
LY294002
(543/458) area/mito area
Chloroquine
Patient 1
iii
Pat 2
Rapamycin
LY294002
Patient 2
D
ARMS-qPCR (%)
ns
Chloroquine
A549 Cybrid Cells
A549 Cybrids
Rapamycin
LY294002
E
Patient 1
Pat 1
F
Inositol phosphates
Phosphatidylinositol
Glucose
PPP
Lipid synthesis
NAD+
NADH
Pyruvate
Lactate
Acetyl-CoA
Oxaloacetate
Citrate
TCA cycle
α-KG
Glutamine
Cholesterol ester
Sphingomyelin
NADH/NAD+
ROS
Mutant
WT
UPRmt
Δψm
O2
H2O
NAD+
LY294002
MK2206
Rapamycin
PI3K/AKT/mTORC1
autophagy inhibition
Fusion
Fission
Mitophagy
lysosome damage

Figure S7

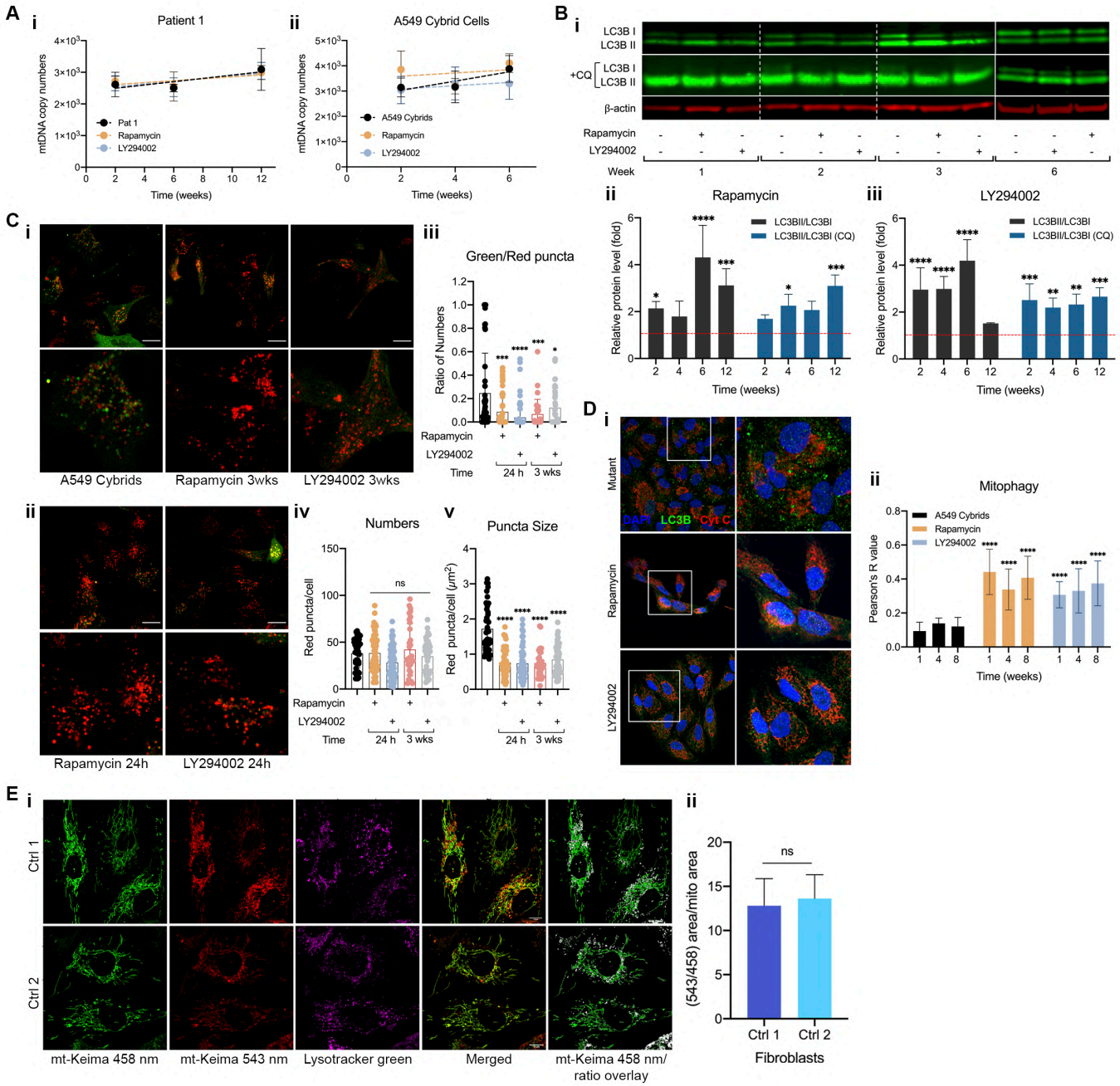
A
i
Patient 1
mtDNA copy numbers
Pat 1
Rapamycin
LY294002
Time (weeks)
ii
A549 Cybrid Cells
A549 Cybrids
Rapamycin
LY294002
Time (weeks)
B
i
LC3B I
LC3B II
+CQ
β-actin
Rapamycin
LY294002
Week
ii
Rapamycin
iii
LY294002
Relative protein level (fold)
LC3BII/LC3BI
LC3BII/LC3BI (CQ)
Time (weeks)
C
i
A549 Cybrids
Rapamycin 3wks
LY294002 3wks
iii
Green/Red puncta
Ratio of Numbers
Rapamycin
LY294002
Time
24 h
3 wks
ii
Rapamycin 24h
LY294002 24h
iv
Numbers
Red puncta/cell
ns
v
Puncta Size
Red puncta/cell (μm²)
D
i
Mutant
Rapamycin
LY294002
DAPI
LC3B
Cyt C
ii
Mitophagy
A549 Cybrids
Rapamycin
LY294002
Pearson's R value
Time (weeks)
E
i
Ctrl 1
Ctrl 2
mt-Keima 458 nm
mt-Keima 543 nm
Lysotracker green
Merged
mt-Keima 458 nm/
ratio overlay
ii
(543/458) area/mito area
ns
Ctrl 1
Ctrl 2
Fibroblasts

506 **FIGURE LEGENDS**

507 **Figure 1. The m.3243A>G mtDNA mutation causes mitochondrial dysfunction and switches cell**
508 **metabolism to a more glycolytic phenotype, resulting in redox imbalance and oxidative stress.**

509 (A) PCR-RFLP and ARM-qPCR were used to quantify the mutation load for patient-derived fibroblasts
510 (n = 3 independent biological samples) and A549 cybrid cells (n = 5 independent biological samples).

511 (B-D) Cell respiratory capacity was measured using the Seahorse XFe96 extracellular flux analyser in
512 patient fibroblasts (B, n = 6 culture wells) and A549 cybrid cells (C, n = 9 culture wells, further
513 normalised to mtDNA copy number), showing a major decrease in oxygen consumption under all
514 conditions. (D) oxygen consumption dependent on ATP production– the response to oligomycin – is
515 plotted.

516 (E) The expression of respiratory chain proteins and supercomplex assembly in patient fibroblasts
517 assessed using blue native gels electrophoresis (BNGE, i) and quantified (ii), showing a major decrease
518 in the assembly of all supercomplexes from the patient-derived cells (n = 3 independent experiments)

519 (F) The mitochondrial membrane potential of fibroblasts was measured using TMRM with confocal
520 microscopy (i) and quantified (ii), showing a significant decrease in potential (n = 5 independent
521 experiments). The images were further analysed using the mitochondrial fragmentation count (MFC)
522 for mitochondrial morphology (iii), confirming the impression of a fragmented phenotype (n=25 cells).
523 Scale bar = 50 μm.

524 (G) ROS production rates of patient fibroblasts were measured using the reporters, DHE (i) and
525 MitoSOX (ii). Rates of production were significantly increased in patient-derived cells (n = 6
526 independent biological samples).

527 (H) The growth rates of patient fibroblasts were measured under a range of different nutrient
528 conditions (normalised to the growth rate of each cell line in regular cell media), showing a decrease
529 of growth rate compared to controls at glucose concentrations of 5 and 1 mM (i) but not at low
530 glutamine (ii) concentrations (n = 6 culture wells for all conditions, 3 independent experiments).

531 (I) Glucose uptake in patient fibroblasts was measured using the fluorescent glucose analogue, 2-
532 NBDG, showing a significantly increased rate of glucose uptake in the patient fibroblasts (n = 15 culture
533 wells).

534 (J) Schematic depicting the simplified mechanism that maintains cytosolic NADH:NAD^+ balance.

535 (K) NADH:NAD^+ ratio of fibroblasts was measured using the reporter, SoNar, under basal conditions
536 and after addition of pyruvate (200 μM, 30 min; i) and quantified (ii; n = 50±10 cells). Scale bar=100
537 μm.

538 (L) Lactate production (normalized to glucose consumption) was measured in the media of fibroblasts
539 using CuBiAn and showed a significant increase in lactate release in the media of patient-derived cells
540 (n = 4 independent biological samples).

541 All data are represented as mean ± s.d. and data were analysed by one/two-way ANOVA with Tukey's
542 multiple comparisons test for fibroblasts and by unpaired t test for cybrid cells (* $p < 0.05$, ** $p < 0.01$,
543 *** $p < 0.001$, **** $p < 0.0001$).

544

545 **Figure S1. The metabolic phenotype of A549 cybrid cells recapitulates the metabolic features of**
546 **patient fibroblasts.**

547 (A) Mitochondrial DNA copy number (ii, n = 5 independent biological samples) of A549 cybrid cells.

548 (B) The mitochondrial membrane potential of A549 cybrid cells measured using TMRM with confocal
549 imaging (scale bar=20 μm, n = 7 independent biological samples).

550 (C-D) Rates of ROS production in A549 cybrid cells and the parental cells were measured using
551 dihydroethidium (DHE), as the rate of increase in red fluorescence intensity over 80 min incubation
552 with DHE. (D) ROS production rates of A549 cybrid cells reported by DHE (i, n = 9 independent
553 biological samples) and MitoSOX (ii, n = 3 independent biological samples).

554 (E-G) A scheme describing how growth rates were obtained by fitting growth curves with an
555 exponential cell growth model (E). Based on the model, growth rate of fibroblasts (n = 3 culture wells)
556 and A549 cybrid cells cultured with regular medium were obtained (n = 5 culture wells, $p = 0.84$; F).
557 (G) Cell growth rates of A549 cybrid cells were measured under a range of different nutrient conditions
558 (normalised to the growth rate of each cell line in regular cell media), showing a decreased rate of
559 growth of A549 cybrid cells compared to controls at glucose concentrations of 5 and 1 mM (i; n = 10
560 culture wells) but not at low glutamine (ii) concentrations (n = 6 culture wells).

561 (H) Glucose uptake in A549 cybrid cells was measured by 2-NBDG, showing a significantly increased
562 rate of glucose uptake in the cybrid cells compared to A549 controls (n=21 culture wells).

563 (I) Schematic depicting the ratiometric probe for NADH:NAD^+, SoNar.

564 (J) NADH:NAD^+ ratio of A549 cybrid cells under basal condition and after addition of pyruvate (200
565 μM, 30 min; i) was measured by the probe and quantified (ii; n = 180 cells).

566 (K) pH in the media from patient fibroblasts cultured for 2 days was measured based on the ratiometric
567 property of the pH indicator in media, phenol red, and showing a lower pH in the media of patient
568 fibroblasts than that of controls (n = 6 independent biological samples).

569 All data are represented as mean ± s.d. and were analysed by one/two-way ANOVA with Tukey's
570 multiple comparisons test for fibroblasts and by unpaired t test for cybrid cells (* $p < 0.05$, ** $p < 0.01$,
571 *** $p < 0.001$, **** $p < 0.0001$).

572

573 **Figure 2. The m.3243A>G mutation rewires glucose and lipid metabolism towards increased**
574 **anabolic biosynthesis and lipid accumulation.**

575 (A) The concentration of metabolites obtained by GC-MS was used to determine the enriched
576 metabolic pathways in patient fibroblasts by MetaboAnalyst 4.0., suggesting that phospholipid
577 biosynthesis, PPP, glycolysis, TCA cycle, etc. were enriched (n = 6 technical replicates.).

578 (B) Schematic of simplified glucose metabolism of the cells (i) Red arrows, upregulated pathways or
579 reactions; three yellow circles of pyruvate and beyond, pyruvate is converted to OAA by pyruvate
580 carboxylase; three or two grey circles of pyruvate and beyond, pyruvate is converted to acetyl-CoA by
581 PDH. Tracing the distribution and abundance of ^{13}C enrichment in the intermediates of glycolysis (ii-
582 viii) and the TCA cycle (ix-xiv) combined with Fig S2A revealed an increase in lipid synthesis and PC
583 activity (n = 4 independent biological samples).

584 (C) Immunoblotting (i) of the expression of pyruvate carboxylase and phosphorylation state of PDH
585 showed an increase of pyruvate carboxylase expression and increased phosphorylation of PDH (which
586 reduces its activity) in patient fibroblasts (ii) and A549 cybrid cells (iii) (n = 3 independent experiments
587 for all cell lines).

588 (D) Nile Red O staining (i) showing the numbers (ii) and area (iii) of lipid droplets in patient fibroblast
589 (n = 20 cells). Scale bar = 50 μm.

590 (E) Lipid profiles of patient fibroblasts acquired by LC-MS were analysed by MetaboAnalyst 4.0.,
591 showing a strikingly increased content of Inositol phosphate, cholesterol esters and sphingomyelin (n
592 = 6 independent biological samples). GPC, glycerophosphatidylcholines. TAG, triacylglycerols. GPE,
593 glycerophosphatidylethanolamines. GPI, glycerophosphatidylinositols. SM, sphingomyelins.

594 All data, except Figs. 2A and 2E, are represented as mean ± s.d. and were analysed by one/two-way
595 ANOVA with Tukey's multiple comparisons test for fibroblasts and by unpaired t test for cybrid cells
596 (* $p < 0.05$, ** $p < 0.01$, *** $p < 0.001$, **** $p < 0.0001$).

597

598 **Figure S2. The metabolomic and lipidomic profiles of fibroblasts carrying the m.3243A>G mutation**
599 **are distinct from that of their matched controls.**

600 (A) The heatmap of metabolite concentrations obtained by GC-MS was generated by MetaboAnalyst
601 4.0 (n = 3 technical replicates), revealing significant differences in the concentrations of several
602 metabolites between controls and patient fibroblasts.

603 (B) PLS-DA for the dataset of Fig. S2A showed that the metabolic profiles of patient fibroblasts were
604 distinct from that of controls.

605 (C) A reduced incorporation of ^{13}C into serine (i) and glycine (ii) and an increase of serine concentration
606 (Fig S2A) in the patient cells (mean ± s.d, of n = 4 independent biological samples).

607 (D) Metabolite set enrichment analysis based on computational enzyme knockout model predicted
608 that pyruvate carboxylase was affected ($p < 0.05$).

609 (E-F) PLS-DA (E) and enriched metabolic pathways (F) for the dataset of Fig. 2E.

610 All data were analysed as stated above (* $p < 0.05$, ** $p < 0.01$, *** $p < 0.001$, **** $p < 0.0001$)

611

612 **Figure 3. The PI3K-Akt-mTORC1 axis is upregulated in the m.3243A>G mutant cells, prompting**
613 **ISR/UPR^{mt} response and perturbing autophagy.**

614 (A) Analysis of RNA-seq data from the patient fibroblasts by QIAGEN Ingenuity Pathway Analysis (IPA)
615 showed the enriched metabolic pathways ($p < 0.05$), matching the findings shown in Figs. 1 and 2.

616 (B) RNA-seq of patient fibroblasts analysed by IPA showed cell signalling pathways which are enriched
617 in cells carrying the m.3243A>G mutation. These include striking and significant increases in
618 expression of pathways involving PI3K-Akt, mTOR, EIF2, and NRF2. It is notable also that PTEN
619 expression, a negative regulator of PI3K-Akt-mTOR signalling was downregulated ($p < 0.05$, Z-score >
620 1; Blue, inhibited; Red, activated).

621 (C) Immunoblotting of p-Akt/Akt (i-ii), p-S6/S6 (iii) and p-AMPK/AMPK (iv) in patient fibroblasts grown
622 in the presence of 10% or 1% FBS media, showing a major increase in p-Akt/Akt and p-S6/S6 in the
623 presence of 1% FBS media in the mutant cells (mean ± s.d. of n = 3 independent experiments).

624 (D) A simple scheme showing the regulation of autophagy and protein translation by the PI3K-Akt-
625 mTORC1 pathway.

626 (E) Immunoblotting of LC3B with chloroquine (CQ, 50 μM for 5 h; n = 4 independent biological samples)
627 or without CQ (n = 7 independent biological samples) in patient fibroblasts (i) and quantified in (ii)
628 suggests an accumulation of LC3BII in the patient cells without an increase in autophagic flux.

629 (F) confocal imaging of live cells transfected with the autophagy reporter, mCherry-GFP-LC3 in patient
630 fibroblasts (i, n=20 cells). The ratio of green/red puncta (ii), autophagosome numbers (iii) and puncta
631 size (iv) were further quantified, showing an increase of these indices. Scale bar = 50 μm.

632 (G) Immunoblotting of p-eIF2α/eIF2α, ATF4, ATF5 and CHOP in patient fibroblasts (i) showed an
633 increase of expression or phosphorylation of these proteins (ii) (n = 3-8 independent experiment).

634 (H) Immunofluorescence staining for p-AKT/AKT (i, n > 60 muscle fibres) and p-S6/s6 (ii, n > 25 muscle
635 fibres) in patient muscle biopsies confirmed the increased phosphorylation of Akt and S6 in the
636 patients (iii). The mutant loads of the m.3243A>G mutation in biopsies were quantified by ARMS-
637 qPCR. Scale bar = 100 μm.

638 (I) Re-analysis of a published RNA-seq data set of patient biopsies collected by Deng *et al.* using IPA
639 confirmed the enrichment of metabolic pathways identified in patient-derived fibroblasts ($p < 0.05$).

640 All data, except Figs. 3A-B and 3I, are represented as mean ± s.d. and were analysed by one/two-way
641 ANOVA with Tukey's multiple comparisons test for fibroblasts and by unpaired t test for biopsies (* p
642 < 0.05, ** $p < 0.01$, *** $p < 0.001$, **** $p < 0.0001$).

643

644 **Figure S3. Analysis for RNA-seq of patient fibroblasts and the enriched metabolic pathways**
645 **recapitulates the metabolic phenotype of patient fibroblasts.**

646 (A-C) RNA-seq showed by a heatmap (A), a volcano plot (B) and 3D-PCA (C). Gene expression in the
647 mutant cells was significantly distinct from both of the controls: 3394 genes were differentially
648 expressed (FDR < 0.05, with 1849 up-regulated and 1545 down-regulated)

649 (D) Analysis of the RNA seq data showing a general decrease in mRNA expression of OxPhos-related
650 genes in patient fibroblasts.

651 (E-F) Analysis of the RNA-seq data showing an altered mRNA expression in antioxidant defence-related
652 genes (E), a reduced mRNA expression of genes involving in the cholesterol synthesis and an altered
653 inositol phosphate metabolism in patient fibroblasts (F).

654 (G) The mRNA expression of TCA cycle and glycolysis genes in patient fibroblasts confirmed our
655 findings in Fig 2, such as increased pyruvate carboxylase and HK1 expression.

656

657 **Figure S4. RNA-seq details of patient fibroblasts and supporting results from A549 cybrid cells.**

658 (A) Detailed analysis of the mRNA expression of multiple genes involved in the PI3K-Akt, mTOR and
659 EIF2 pathways in patient fibroblasts, showing consistent differences in a wide array of genes involved
660 in these pathways.

661 (B) Immunoblotting of p-Akt/Akt, p-S6/S6 and p-AMPK/AMPK in A549 cybrid cells shows increased
662 phosphorylation of Akt and S6 but not of AMPK, consistent with the results of fibroblasts (mean ± s.d.
663 of n = 4-5 independent experiments, two-way ANOVA with Tukey's multiple comparisons test).

664 (C) Immunoblotting of LC3B with CQ (50 µM for 5 h; n = 4 independent biological samples) or without
665 CQ (n = 10 independent biological samples) in A549 cybrid cells (ii) suggests an accumulation of LC3BII
666 without an increase in autophagic flux (iii) as seen in the patient fibroblasts (mean ± s.d., two-way
667 ANOVA with Tukey's multiple comparisons test)

668 (D) Imaging of mCherry-GFP-LC3 (n>20 cells) in A549 cybrid cells (i). The ratio of green/red puncta (ii,
669 p = 0.0375), autophagosome numbers (iii, p = 0.1640) and puncta size (iv, p = 0.0219) were further
670 quantified, showing an increase of green/red puncta and puncta size in the patient cells (mean ± s.d.,
671 unpaired t test for all analyses). Scale bar = 30 µm.

672 (E) Immunoblotting of p-eIF2α/eIF2α, ATF4, ATF5 and CHOP in A549 cybrid cells showed increased
673 expression of all of these proteins, consistent with the results from the patient fibroblasts (mean ± s.d.
674 of n = 5-8 independent experiments, two-way ANOVA with Tukey's multiple comparisons test).

675 All data were analysed as stated above (* p<0.05, ** p<0.01, *** p<0.001, **** p<0.0001).

676

677 **Figure 4. Inhibitors of PI3K, Akt, and mTORC1 reduce mutation load, rescue mitochondrial function**
678 **and reduce glucose dependence.**

679 (A-B) Schematic depicting pharmacological inhibition of the PI3k-Akt-mTORC1 pathway by rapamycin
680 (RP) or LY290042 (LY) (A). (B) Sustained treatment of cells over 6 or 12 weeks with rapamycin (5 µM)
681 or LY290042 (5 µM) caused a progressive decrease in mutant mtDNA load in A549 cybrid cells (i) and
682 fibroblasts of patient 1 (ii) and suppressed the progressive increase of mutant load with time in culture
683 seen in patient 2 fibroblasts (iii) (n = 3 independent experiments). The concentrations of RP and LY
684 here refer to all subsequent treatments.

685 (C) Immunoblotting of the phosphoproteins (p-Akt/Akt, p-mTOR/mTOR and p-AMPK/AMPK; i) and
686 ISR/UPR^{mt} proteins (ii) in patient 1 fibroblasts treated with RP (iiI) or LY (iv) over 12 weeks

687 demonstrated the effective inhibition of Akt or mTORC1 and an amelioration of the integrated stress
688 response (ISR) in the drug-treated cells (n = 3-4 independent experiments).

689 (D) The mitochondrial membrane potential of patient 1 fibroblasts treated with LY or RP for 12 weeks
690 were significantly increased (ii) and mitochondrial fragmentation counts (MFC, iiI) were also
691 significantly reduced (n = 15 independent biological samples). Scale bar = 50 μm.

692 (E) The respiratory capacity of patient 1 fibroblasts treated with LY or RP for 12 weeks was measured
693 using the Seahorse XFe96 extracellular flux analyser and showed a major increase in oxygen
694 consumption under all conditions for the drug-treated cells (n = 15 of culture wells).

695 (F) The $NADH/NAD^+$ ratio of patient 1 fibroblasts treated with LY or RP for 12 weeks was measured
696 under basal condition and pyruvate (i, 200 μM, 30 min) and quantified (ii; n > 180 cells). The result
697 showed a significant decrease compared to pre-treatment levels. Scale bar = 100 μm.

698 (G) Acidification of the growth medium revealed by the absorption ratio of phenol red was significantly
699 reduced after chronic drug treatments with RP and LY (i and ii; n = 9 culture wells). Lactate production
700 normalised to glucose consumption (iii, n = 4 culture wells) was also significantly reduced. In each
701 case, media were collected after 2 days culture of patient 1 fibroblasts treated with LY or RP for 12
702 weeks.

703 (H) Fibroblasts of patient 1 treated with LY or RP for 12 weeks were also cultured in media with a
704 variety of glucose/galactose concentrations to further assess the glucose dependence, displayed a
705 significant improvement of cell growth in all conditions from the drug-treated cells (n = 4-8 culture
706 wells).

707 (I) BNGE were used to assess the expression of respiratory chain proteins and supercomplex assembly
708 of patient 1 fibroblasts treated with LY or RP, showing a major increase in the assembly of almost all
709 supercomplexes from the drug-treated cells (n = 3 independent experiments).

710 (J) Rates of ROS production of patient 1 fibroblasts treated with LY or RP for 12 weeks were
711 significantly reduced to the level that no longer significantly different from controls, which was shown
712 in Fig. 1G (n = 3 independent experiments).

713 All data represented as mean ± s.d. and were analysed by one/two-way ANOVA with Tukey's multiple
714 comparisons test (* $p < 0.05$, ** $p < 0.01$, *** $p < 0.001$, **** $p < 0.0001$).

715

716 **Figure S5. Inhibition of PI3K, Akt, and mTORC1 also reduced mutant load and rescued mitochondrial**
717 **function in A549 cybrid cells.**

718 (A-B) Immunoblotting (i) of the phosphoproteins (p-Akt/Akt, p-S6/S6 and p-AMPK/AMPK; A) and
719 ISR/UPR^{mt} proteins (B) in A549 cybrid cells treated with RP (ii) or LY (iii) over 6 weeks demonstrate the
720 effective inhibition of Akt or mTORC1 and a decrease of the ISR in the drug-treated cells (n = 3
721 independent experiments).

722 (C) The mitochondrial membrane potential of A549 cybrid cells significantly increased after exposure
723 to LY or RP for 6 weeks (i and ii). Mitochondrial fragmentation counts (MFC, iii) were also reduced
724 following treatment with either compound (n = 5 independent biological samples). Scale bar = 25 μm.

725 (D) Cell respiratory capacity of A549 cybrid cells treated with LY or RP for 6 weeks was measured using
726 the Seahorse XFe96 extracellular flux analyser, and showed a major increase in oxygen consumption
727 under all conditions after treatment (n = 18 culture wells).

728 (E-I) MK2206, an inhibitor of pan-Akt (E), treatment (1 μM) also reduced mutant load in A549 cybrid
729 cells over 6 weeks of treatment (F, n = 3 independent experiments). Immunoblotting of p-Akt/Akt and
730 p-S6/S6 (G) confirmed the effect of MK2206 (n = 3 independent samples). Mitochondrial membrane
731 potential (H) and cell respiratory capacity (I, n = 8 culture wells) of A549 cybrid cells also increased
732 after treatment with MK2206.

733 (J) PCR-RFLP was applied to measure the change in mutant load in 143B cybrid cells carrying the
734 m.8993T>G mutation (N80, with 80% mutant mtDNA; N50, with 50% mutant mtDNA) treated with LY
735 or RP for 8 weeks, showing no significant effect on the mutant load of the m.8993T>G (n = 3
736 independent biological samples).

737 (K) Cytosolic NADH:NAD$^+$ ratio of A549 cybrid cells transfected with the genetically encoded probe
738 SoNar and treated with LY or RP for 6 weeks was measured (i) and quantified (ii) under basal condition
739 and following exposure to pyruvate (200 μm, 30 min; n > 30 cells).

740 (L) The absorption ratio of phenol red was used to measure the pH of the growth media (i and ii, n=10
741 culture wells) and the kit of the CuBiAn instrument was used to measure lactate production (iii, n = 4
742 culture wells). Both acidification of the medium and lactate secretion were reduced after 2 days
743 culture of A549 cybrid cells treated with LY or RP for 6 weeks.

744 (M) BNGE were used to measure supercomplex assembly and In Gel activity of A549 cybrid cells after
745 6 weeks of treatment with LY or RP (n = 3 independent experiments).

746 (N) Rates of ROS production of A549 cybrid cells treated with LY or RP for 6 weeks were reduced to
747 the level that no longer significantly different from WT cells, which was shown in Fig. S1C-D (n = 9
748 culture wells).

749 All data represented as mean ± s.d. and were analysed by one/two-way ANOVA with Tukey's multiple
750 comparisons test (* $p < 0.05$, ** $p < 0.01$, *** $p < 0.001$, **** $p < 0.0001$).

751

752 **Figure 5. Reduction of the m.3243A>G mutant load by inhibition of PI3K-Akt-mTORC1 requires**
753 **neither selective cell death nor clonal expansion and is a cell-autonomous event.**

754 (A) A flow chart describing the cell culture process (i) used to assess cell growth/death (ii) over the 4-
755 or 8-weeks drug treatments and single-cell PCR for the m.3243A>G mutant loads using TaqMan SNP
756 genotyping (iii).

757 (B) Cell growth (i and ii) and cell death (iii and iv) over the 4- or 8-weeks drug treatments of A549
758 cybrid cells (i and iii) and patient 1 fibroblasts (ii and iv) were measured using the Incucyte (n=6 culture
759 wells). Although treatment with either LY or RP at 5 μM slowed cell proliferation in both patient 1
760 fibroblasts and cybrid cells (i and ii), the cell death numbers were also lowered by the drug treatments
761 (iii and iv).

762 (C-D) A scatter plot showing the distribution of WT and mutant mtDNA measured in single A549 cybrid
763 cells treated with LY or RP for 4 weeks showed a clear shift of mutant load distribution. (C). Mutant
764 load distributions of single A549 cybrid cells (i, n > 800 cells) and patient 1 fibroblasts (ii n > 500 cells)
765 treated with LY or RP for 4 and 8 weeks, respectively.

766 All data represented as mean ± s.d. and were analysed by one/two-way ANOVA with Tukey's multiple
767 comparisons test (* $p < 0.05$, ** $p < 0.01$, *** $p < 0.001$, **** $p < 0.0001$).

768

769 **Figure S6. TaqMan SNP genotyping can be used at single-cell resolution to measure the distribution**
770 **of mutant mtDNA burden in a cell population.**

771 (A) Cell growth and cell death of A549 cybrid cells were measured before and after treatment with MK
772 for 4 weeks (n = 8 culture wells). The drug had no specific effect on the mutant cells.

773 (B-C) TaqMan SNP genotyping was validated by measuring the mutation load in a whole population of
774 cells (B, n = 3 independent biological samples) and then to establish the range of mutant load at the
775 level of single cells in the A549 cybrid cells (C).

776 (D) Immunofluorescence staining for COXIV (i and quantified in ii) showed that the expression of COXIV
777 in patient 1 fibroblasts was significantly lower than that of control 1 (n = 100 cells), while LY or RP
778 treatments restored its expression (iii, n > 60 of cells). The histograms (iv and v) display the

779 heterogeneous distribution of intensities measured at the single-cell level in control 1 and patient 1
780 fibroblasts.

781 All data are represented as mean ± s.d. and were analysed by one/two-way ANOVA with Tukey's
782 multiple comparisons test (* $p < 0.05$, ** $p < 0.01$, *** $p < 0.001$, **** $p < 0.0001$).

783

784 **Figure 6. Autophagy/mitophagy is necessary to reduce the m.3243A>G mutant load following**
785 **inhibition of the PI3K-Akt-mTORC1 pathway.**

786 (A) In fibroblasts of patient 1, immunoblotting (i) of LC3B with or without CQ (50 μm for 5 h on the
787 day of experiments) over 12 weeks drug treatments (ii and iii) showed a major increase in autophagic
788 flux in drug-treated cells (n = 3 of independent experiments).

789 (B) Confocal imaging of the autophagy reporter, mCherry-GFP-LC3 (n = 25 cells) in patient 1 fibroblasts
790 treated with LY or RP at the indicated time points (i, 6 weeks, and ii, 24 h). The ratio of green/red
791 puncta (iii), autophagosome numbers (iv) and puncta size (v) were further quantified, showing a major
792 decrease in the ratio of green/red puncta and puncta size in response to the treatments. Scale bar =
793 50 μm.

794 (C) Imaging of the mitophagy reporter (i), mitoKeima, was used to specifically quantify mitophagy in
795 patient fibroblasts treated with LY, RP or CQ (10 μM). Quantification of the mitochondrial area fraction
796 engulfed in autolysosomes in both patient 1 (ii) and 2 (iii) were quantified and showed a dramatic
797 increase in mitophagy in both patient cell lines, which was completely prevented by treatment with
798 chloroquine (n = 7-10 independent biological samples).

799 (D-E) A549 cybrid cells (D) and patient 1 fibroblasts (E) were cultured with the inhibitors RP and LY as
800 in all prior experiments but in combination with CQ (10 μM), showing that CQ completely prevented
801 the decrease of mutant load in response to inhibition of the PI3K-Akt-mTORC1 pathway (n = 3
802 independent experiments).

803 (F) A scheme describing how the m.3243A>G mutation alters cell metabolism, including mitochondrial
804 dysfunction, altered glucose metabolism, redox imbalance and oxidative stress, which leads to the
805 constitutive activation of the PI3K-Akt-mTORC1 pathway and a defect in autophagy/mitophagy.
806 Pharmacological inhibition of this pathway reduces mutant load, rescues mitochondrial function and
807 reduces glucose dependence. These findings suggest that the activation of the PI3K-Akt-mTORC1
808 pathway drives a positive feedback cycle, which maintains/increases mutant mtDNA, augments the
809 metabolic rewiring and thus worsens cell signalling perturbation. This positive feedback loop may
810 shape the phenotype of the disease and determine disease progression.

811 All data are represented as mean ± s.d. and were analysed by one/two-way ANOVA with Tukey's
812 multiple comparisons test (* $p < 0.05$, ** $p < 0.01$, *** $p < 0.001$, **** $p < 0.0001$).

813

814 **Figure S7. Mitochondrial biogenesis and changes in mtDNA copy number do not explain the**
815 **reduction of mutant mtDNA burden, while autophagy/mitophagy is also upregulated by inhibition**
816 **of the PI3K-Akt-mTORC1 pathway in A549 cybrid cells.**

817 (A) Quantitative PCR assessing mtDNA copy numbers of patient 1 fibroblasts (i) and A549 cybrid cells
818 (ii) over the 6- or 12-weeks of treatments (n = 3 independent experiments).

819 (B) In A549 cybrid cells, immunoblotting of LC3B with or without CQ (50 μm for 5 h on the day of
820 experiments) throughout drug treatments (i) showed a major increase in autophagic flux in drug-
821 treated cells (ii and iii, n = 3 independent experiments).

822 (C) Imaging of mCherry-GFP-LC3 (n > 30 cells) in A549 Cybrid cells treated with LY or RP at the indicated
823 time points (i and ii). The ratio of green/red puncta (iii), autophagosome numbers (iv) and puncta size
824 (v) were further quantified, showing a major decrease in the ratio of green/red puncta and puncta
825 size. Scale bar = 20 μm.

826 (D) Immunofluorescence staining for LC3B and cytochrome c (i) indicating that mitophagy of A549
827 cybrid cells was increased by LY or RP treatments (ii, n > 40 cells).

828 (E) Imaging of mtKeima (i) showing that mitophagy of WT fibroblasts (ii) was much higher than patient
829 fibroblasts (compared with Fig. 6C, ii and iii).

830 All data are represented as mean ± s.d. and were analysed by one/two-way ANOVA with Tukey's
831 multiple comparisons test (* $p < 0.05$, ** $p < 0.01$, *** $p < 0.001$, **** $p < 0.0001$).

832 **METHODS**

833 **RESOURCE AVAILABILITY**

834 **Lead Contact**

835 Further information and requests for resources and reagents should be directed to and will be fulfilled
836 by the Lead Contact, Michael R Duchen (m.duchen@ucl.ac.uk).

837

838 **Materials Availability**

839 This study did not generate new unique reagents.

840

841 **Data and Code Availability**

842

843 **EXPERIMENTAL MODEL AND SUBJECT DETAILS**

844 **Cell Lines**

845 The A549 cybrid cell line derived from the fusion of enucleated patient cells harbouring the
846 m.3243A>G mtDNA mutation was a gift from Ian Holt (Biodondostia Research Institute, San Sebastián,
847 Spain). The 143B cybrid cell lines with ~50% and ~80% of the m.8993T>G mtDNA mutant loads were
848 gifts from the Minczuk lab (MRC Mitochondrial Biology Unit, Cambridge, UK). Control and patient
849 fibroblasts bearing the m.3243A>G mtDNA mutation were obtained from the MRC Centre for
850 Neuromuscular Disorders Biobank London. The patient fibroblasts with the m.3243A>G mutation
851 were isolated from two female subjects (mother and daughter) at the age of 59 (patient 1) and 35
852 (patient 2) at the time biopsies were taken. For patient 1, the clinical symptoms included diabetes,
853 myoclonus, sensorineural hearing loss, memory decline, myopathy, pigmentary retinopathy and
854 bipolar affective disorder. For patient 2, the symptoms included diabetes, sensorineural deafness,
855 cerebellar ataxia, myopathy, epilepsy, depression and cognitive impairment. These cell lines were
856 cultured in Dulbecco's modified Eagle's medium (Gibco #10566016) supplemented with 10% fetal
857 bovine serum (Gibco #16140071), and 1% Antibiotic-Antimycotic (Gibco #15240096) and incubated at
858 37 °C with 5% CO_2.

859

860 **Human muscle biopsies**

861 The muscle biopsies were from a female patient with the m.3243A>G mutation (at the age of 55) and
862 a matched healthy control. The study was approved by the Queen Square Research Ethics Committee,
863 London (09/H0716/76). Informed consent was obtained from all participants.

864

865 **METHOD DETAILS**

866 **Cell culture and drug treatments for PI3K, Akt, or mTORC1 inhibition**

867 A549 cybrid cells (WT and mutant) and 143B cybrid cells were passaged every 3-4 days at 80%
868 confluence and trypsinised using 0.25% trypsin-EDTA (Gibco #25200056). Similarly, control and
869 patient fibroblasts were passaged every week in the same way. Media with or without drugs were
870 changed every 2-3 days. For drug treatments, rapamycin (Cayman Chemical #13346), LY294002
871 (Cayman Chemical #70920) and MK2206 (Cayman Chemical #11593) were dissolved in DMSO (Sigma-
872 Aldrich #D2650) at 10 mM stock concentrations, while chloroquine (Cayman Chemical #14194) was
873 dissolved in PBS at 50 mM for stock. Drugs were subsequently diluted to their working concentrations
874 in media. Heteroplasmy level in the A549 cybrid cells, the 143B cybrid cells and the fibroblasts of
875 patient 1 without treatments did not change significantly throughout the study as assessed by ARMS-
876 qPCR or PCR-RFLP.

877

878 **Measurements for mtDNA mutations**

879 Levels of mtDNA mutation were detected using PCR-restriction fragment length polymorphism
880 (RFLP)[16,55] or allele refractory mutation system (ARMS)-based quantitative PCR (qPCR) analysis [17]. DNA
881 extractions from frozen cells were performed using the DNeasy Blood & Tissue Kit (Qiagen #69506).
882 Concentrations of DNA samples were quantified using NanoDrop. All primer pairs used can be found
883 in the Key Resources Table. For PCR-RFLP, samples (20 ng/µl, 2 µl) were mixed with the master mixes
884 containing 1 µl primers (10 µM each) and reagents of GoTaq G2 (Promega #M7845) and the final
885 volume was 25 µl. After 30 thermocycles, amplified PCR products (8 µl) were further digested by ApaI
886 (Promega #R6361) for the m.3243A>G and HapII (Promega #R6311) for the m.8993T>G and analysed
887 by a 2% agarose gel with ethidium bromide. Densitometric analysis was performed by Fiji [56]. For ARMS-
888 qPCR, samples were diluted to 0.4 ng/µl. ARMS primer working solutions (5 µM, 1 µl each) and SYBR
889 Green JumpStart Taq ReadyMix (Sigma-Aldrich #S4438) were added together as master mixes for
890 mutant and wild-type genes. DNA samples (3 µl) and master mixes (7 µl) were pipetted into a 96-well

891 PCR plate (Bio-Rad #MLL9651) and PCR amplification performed using the CFX96 Touch Real-Time PCR
892 Detection System (Bio-Rad). Each sample has three technical replicates. Mutant heteroplasmy level
893 (%) was calculated using $1/[1 + (1/2)^{\Delta CT}] \times 100\%$, where ΔC_T (cycle threshold) = $CT_{wild\text{-}type} - CT_{mutant}$.

894

895 **Quantification of relative mtDNA copy number**

896 The relative mtDNA copy number of cells was determined using quantitative PCR with primers for the
897 mtDNA $tRNA^{Leu(UUR)}$ and with primers for the nuclear B2-microglobulin as previously described [57].
898 Standard 96 well PCR plate with optically clear sealing film and CFX96 Real-Time PCR Detection System
899 (Bio-Rad) were used. PCR mix consists of 2 µl of template DNA (3 ng/µl), 2 µl of primer pair (final
900 concentration of 400 nM), 12.5 µl of SYBR Green JumpStart Taq ReadyMix (Sigma-Aldrich) and 8.5 µl
901 of DNase/RNase free H_2O. The thermal cycling conditions were as follow: 50 °C for 2 min, 95 °C for 10
902 min and then 40 cycles of 95 °C for 15 s and 62 °C for 1 min. Each sample has three technical replicates.
903 The following equation was used to determine the relative mitochondrial DNA content, $2 \times 2^{\Delta CT}$, where
904 ΔC_T is nuclear DNA CT value subtracted by mtDNA CT value.

905

906 **The mitochondrial oxygen consumption rate**

907 Measurements of aerobic respiration and glycolysis were conducted with the Seahorse Bioscience
908 XFe-96 bioanalyzer using the Seahorse XF Cell Mito Stress Test Kit (Agilent #103015-100). Cells were
909 seeded on XF96 cell culture microplates (Agilent #102416-100) two days before the experiment (A549
910 cybrid cells, 1×10^4 cells/well; Fibroblasts, 2×10^4 cells/well). On the day of the experiment, the culture
911 medium was replaced with Seahorse XF Base medium (Agilent #103334-100) supplemented with 1
912 mM pyruvate (Gibco #11360070), 2 mM glutamine (Gibco #25030081) and 10 mM glucose (Gibco
913 #A2494001) and incubated for 30 min at 37 °C in a CO_2-free incubator before loading into the Seahorse
914 Analyzer. After measuring basal respiration, the drugs oligomycin (5 µM), FCCP (1 µM, 2 µM), and
915 rotenone/antimycin A (0.5 µM/0.5 µM) were added to each well in sequential order. Data were
916 analysed using the XF Cell Mito Stress Test Report Generator. After the assay, cells were stained with
917 Hoechst 33342 (5 µM; Thermo Scientific #62249) for 30 min. ImageXpress was then used to count the
918 numbers of cell nuclei (cell numbers) in each well. The normalisation of the experiments is based on
919 the relative cell numbers obtained.

920

921 **Mitochondrial membrane potential, $\Delta\psi_m$, and the mitochondrial fragmentation count**

922 Cells were seeded (3 x 10^4/well for A549 cybrid cells; 1 x 10^4/well for fibroblasts) in glass-bottom 24-
923 well plates, 2-3 days before imaging. Cells were washed twice with the recording medium, which was
924 phenol red-free DMEM (Gibco #A1443001) with 10 mM glucose, 1 mM glutamine, 10 mM HEPES,
925 adjusted to pH 7.4; and then incubated with 25 nM tetramethylrhodamine methyl ester (TMRM) for
926 30 min at 37 °C. Cells were imaged with an LSM 880 (Carl Zeiss) confocal microscope using Fluar
927 63x/1.40 oil immersion objective lens at 37 °C. TMRM was excited with a 561 nm Argon laser with an
928 output power of 0.2 mW. MBS 488/561 was used as a beam splitter and emitted fluorescence
929 collected at 564-740 nm. Images were acquired using Zen Black software (Carl Zeiss) and fluorescence
930 intensity was quantified using Fiji with the same threshold across all samples. To quantitatively
931 describe mitochondrial morphology, mitochondrial network fragmentation according to Rehman et
932 al., 2012 was applied. Briefly, thresholding images were binarized and mitochondrial structure of each
933 cell was count with the particle counting and normalised to the total mitochondrial area (μm^2) per cell
934 to obtain the mitochondrial fragmentation count (MFC). To be specific, MFC = (number of particles x
935 100)/total mitochondrial area.

936

937 **ROS measurements**

938 Rate of general ROS production was assessed using dihydroethidium (DHE, Invitrogen #D11347), an
939 intracellular superoxide indicator which is oxidised by superoxide to ethidium which fluoresces red.
940 As for mitochondrial ROS production, MitoSOX (Invitrogen #M36008) was used. One day before the
941 experiment, cells were seeded in a glass-bottom 96-well plate (SensoPlate #655892) at a density of 2
942 x 10^4 cells per well. On the day of the experiment, cells were washed twice with PBS and incubated
943 with 5 µM DHE or MitoSOX in recording medium (phenol red-free DMEM, 10 mM glucose, 1 mM
944 glutamine, 10 mM HEPES, adjusted to pH 7.4). Measurements of fluorescence intensity were taken at
945 intervals of 5 min at 37 °C using the CLARIOstar microplate reader (excitation/emission = 518/606 nm
946 for DHE excitation/emission = 510/580 nm for MitoSOX). The total incubation time for DHE is 1 h and
947 30 min for MitoSOX. The slope of fluorescence intensity was calculated (Fig. S1C) and represents the
948 rate of ROS production.

949

950 **Glucose uptake using 2-NBDG**

951 A fluorescent deoxyglucose analogue, 2-NBDG (Invitrogen #N13195), was employed as a probe to
952 measure rates of glucose uptake by cultured cells. Cells were seeded in a glass-bottom 96-well plate
953 as ROS measurements. On the day of experiments, cells were firstly washed with glucose-free
954 recording media twice and incubated with the glucose-free media for 1 h. After media aspiration,
955 recording media with 2-NBDG (100 µg/ml) were then added into wells and incubated for 30 min. After
956 the incubation, cells were then again washed with glucose-free recording media twice and
957 fluorescence intensity were measured using the CLARIOstar microplate reader (excitation/emission =
958 467/542 nm).

959

960 **Medium pH values**

961 Medium pH values were measured based on the ratiometric property of phenol red, a common pH
962 indicator in media. The absorbance of phenol red change in response to changing pH. Cells were
963 seeded in 96-well plates at a density of 1 x 10^4 cells per well with 200 µl media and cultured for 2 days.
964 On the day of experiments, media of each well were then transferred to a new 96-well plate and
965 measured the absorbance of phenol red at 443 and 570 nm immediately. The higher the absorbance
966 ratios of 443 to 570 nm, the more acidic the media.

967

968 **Glucose and lactate concentrations in media using CuBiAn**

969 Media for pH measurements were then directly used for quantifying glucose and lactate
970 concentrations in media. Samples and fresh media were measured using the CuBiAn HT-270
971 biochemistry analyser (Optocell technology) with its Glucose (#200106) and Lactate Assay Kits
972 (#200115) according to manufacturer instructions.

973

974 **Blue native gel electrophoresis (BNGE) and In Gel activity assays**

975 Mitochondria were isolated from cultured fibroblasts and cell lines according to the method described
976 earlier (ref). Digitonin-solubilized mitochondria proteins (100 µg) were separated on pre-cast 3%-12%
977 gradient blue native gels (Invitrogen #BN1001) according to manufacturer's instructions. After
978 electrophoresis, the gels were electroblotted onto PVDF membrane (Millipore #IPVH00010) and
979 probed with anti-OxPhos antibody cocktail (1:1000, Invitrogen #45-8199), anti-SDHA (1:1000, Abcam
980 #ab137040) and anti-ATP5A (1:1000, Abcam #ab14748). The enzymatic activity of different OxPhos

981 complexes was determined by in-gel assays. For CIV+CI activity, the gels were incubated first in CIV
982 substrate (50 mg diaminobenzidine and 100 mg cytochrome c in 50 mM phosphate buffer, pH 7.4)
983 until brown signal was observed and then incubated in CI substrate (0.1 mg/ml NADH, 2.5 mg/ml
984 Nitrotetrazolium Blue chloride in 100 mM Tris–HCl, pH 7.4) until blue signal appeared. The reaction
985 was stopped with 10% acetic acid and the gels were washed and scanned.

986

987 **SDS-PAGE and immunoblotting**

988 For immunoblotting, cells were seeded 1-day prior experiments (60 mm plates for the A549 cybrid
989 cells and 10 cm plates for fibroblasts). To assess autophagic flux, cells were replenished with regular
990 media for 1 h to prevent starvation-induced autophagy. After 1 h, treatment conditions resumed
991 either with or without 50 µM chloroquine for 6 h. For other experiments, cells were then washed with
992 ice-cold PBS once and lysed using 150-300 µl RIPA buffer (Sigma-Aldrich #R0278) with one cOmplete™
993 Protease Inhibitor Cocktail (Roche #4693116001) tablet and one PhosSTOP Phosphatase Inhibitor
994 Cocktail (Roche #4906837001) tablet. Cells were then scraped and centrifuged at 16,000 g at 4 °C for
995 30 min. Protein concentration in the supernatant was quantified using the Pierce BCA Assay Kit
996 (Thermo Scientific #23227). For immunoblotting, 30 µg of protein samples in NuPAGE 4x LDS Sample
997 Buffer (Invitrogen #NP0007) and 2% β-mercaptoethanol (Sigma-Aldrich #63689) were boiled at 99ºC
998 for 5 min. Proteins were separated on 4-12% NuPAGE Bis-Tris polyacrylamide gels (Invitrogen
999 #NP0335) immersed in MOPS running buffer (Invitrogen #NP0001) and transferred onto PVDF
1000 membranes (Millipore #IPFL00010). Membranes were then incubated in Intercept (TBS) Blocking
1001 Buffer (Li-COR Biosciences #927-60001) for 1 h at room temperature. After addition of primary
1002 antibodies diluted in the blocking buffer with 0.1% Tween-20, membranes were incubated overnight
1003 at 4ºC on a shaker. Subsequently, membranes were incubated with appropriate secondary antibodies
1004 (Li-COR Biosciences; 1:10000; IRDye® 680RD Goat anti-Mouse IgG, #926-68070; IRDye® 800CW Goat
1005 anti-Rabbit IgG, #926-32211) for 1 h at room temperature before signals were developed with the
1006 LiCOR Odyssey CLx system. Densitometry analysis was performed using Fiji. Details of all the
1007 antibodies used in this study can be found in the Key Resources Table. Following is the antibodies and
1008 dilutions for immunoblotting: Anti-PC (1:1000, Novus Biologicals #NBP1-49536), anti-phospho-PDHA
1009 (1:1000, Millipore #AP1062), anti-PDHA (1:1000, Invitrogen #45-6600), anti-p-Akt (1:1000, Cell
1010 Signaling Technology #9271), anti-Akt (1:3000, Cell Signaling Technology #9272), anti-p-S6 (1:3000,
1011 Cell Signaling Technology #4858), anti-S6 (1:3000, Cell Signaling Technology #2217), anti-p-AMPK
1012 (1:1000, Cell Signaling Technology #2532), anti-AMPK (1:3000, Cell Signaling Technology #2532), anti-
1013 LC3B (1:3000, Cell Signaling Technology #3868), anti-p-eIF2α (1:1000, Cell Signaling Technology

1014 #9721), anti-eIF2α (1:3000, Cell Signaling Technology #9722), anti-ATF4 (1:1000, Cell Signaling
1015 Technology #11815), anti-ATF5 (1:1000, Abcam #ab60126), anti-CHOP (1:1000, Santa Cruz
1016 Biotechnology #sc-7351), and anti-β-actin (1:10000, Santa Cruz Biotechnology #sc-47778).

1017

1018 **Live-cell imaging for cell growth and death using the Incucyte platform**

1019 Cells were seeded at a density of 2,000 cells/well in a 96-well plate one-day prior imaging with regular
1020 cell culture media. For cell growth/death in a variety of nutrient conditions, cells were washed with
1021 PBS twice and then DMEM (Gibco #11966025 or #11960044) with different concentration of glucose,
1022 galactose (Sigma-Aldrich #G5388) or glutamine and 10% dialysed FBS (Sigma-Aldrich #F0392) were
1023 added. For drug treatments, media were then replaced with fresh media with/without drugs along
1024 with 20 nM SYTOGreen Nucleic Acid Stain (Invitrogen #S7572) just before imaging. Images were
1025 acquired using the Incucyte with 20X objective every 2 h for a 3-4 days period. Cell confluency and cell
1026 death numbers were analysis on Incucyte software and sequentially extracted. Rates of cell growth
1027 were analysed by fitting the growth curve to the exponential cell growth model (Fig. S1E) using the
1028 solver in Excel, while cell death was obtained by simply normalising the numbers of dead cells
1029 (SYTOGreen stained) to total cell confluency.

1030

1031 **Measurements of cytosolic NADH:NAD$^+$ using SoNar**

1032 The genetically encoded probes, SoNar for NADH:NAD$^+$ ratio, were developed by and obtained from
1033 the Yang's Lab (Chinese Academy of Sciences) [18]. For A549 cybrid cells, the cells were seeded at the
1034 density of 4 x 10^4/well in glass-bottom 24-well plates two days before transfection. Lipofectamine
1035 3000 (Invitrogen #L3000001) was used for transfection according to the manufacturer's protocol.
1036 Specifically, we used 1 µg DNA and the ratio of p3000 to the 3000 reagent was 2:1. The cells were
1037 imaged two days after transfection in recording media with the LSM 880 microscope using 20x/0.8
1038 objective lens at 37ºC. Both probes were excited at 405 and 488 separately and emitted fluorescence
1039 longer than 535 nm was collected. For fibroblasts, Human Dermal Fibroblasts Nucleofector Kit (Lonza
1040 #VPD-1001) was used for transfection according to the manufacturer's protocol. Specifically, we used
1041 2.5 µg DNA for 5 x 10^5 cells. Similarly, fibroblasts were imaged two days after transfection with the
1042 same conditions as A549 cybrid cells. Images were acquired using Zen Black software (Carl Zeiss) and
1043 analysed using Fiji. Regions of interest (ROI) were generated by thresholding and binarizing images
1044 and average fluorescence intensity in the ROIs for each channel were then measured. Ratios between
1045 the signal excited at 405 nm and 488 nm were calculated.

1046

1047 **Measurement of autophagy and mitophagy using mCherry-EGFP-LC3 and mt-Keima, respectively**

1048 The autophagy reporter, mCherry-EGFP-LC3 (Addgene plasmid #22418), and mitophagy reporter, mt-
1049 Keima (Addgene plasmid #56018) were purchased from Addgene. The procedure of transfection for
1050 A549 cybrid cells and patient fibroblasts was similar to SoNar. Imaging was performed with the LSM
1051 880 microscope using 63x/1.40 oil immersion objective lens at 37 °C. The mCherry-EGFP-LC3 was
1052 excited at 488 and 561 nm separately and emitted fluorescence 500-580 and longer than 600 nm was
1053 collected. Images were acquired using Zen Black software (Carl Zeiss). Numbers and area of
1054 fluorescent particles for each channel were quantified using Fiji by thresholding images. For mt-Keima,
1055 following transfection, the cells were treated as indicated for 24h and imaged via two sequential
1056 excitations (458 nm, green; 561 nm, red) using a 570- to 695-nm emission range. The laser power was
1057 set at the minimum output to allow the clear visualization of the mt-Keima signal and was separately
1058 adjusted for each experimental conditions. At least 10 z-stacks with 0.45 um thickness were acquired
1059 per sample in an experimental set. LysoTracker Green DND-26 (Invitrogen #L7526) was co-imaged
1060 using a 488 nm excitation and a 495-550 nm emission filter, where indicated. The ratio (high F_{543}/F_{458}
1061 ratio area/total mitochondrial area) was used as an index of mitophagy. Ratio (F_{543}/F_{458}) images were
1062 generated using the Ratio Plus plugin in Fiji. High (F_{543}/F_{458}) ratio areas and total mitochondrial area
1063 were binarized, segmented and quantified in Fiji.

1064

1065 **Metabolomics**

1066 Control and patient fibroblasts were plated 24 hrs before the experiment in 10 cm dishes (1 x 10^6
1067 cells/dish). On the day of experiments, the medium was replaced with phenol red-free DMEM with 1
1068 mM glutamine, 10% dialysed FBS (prepared as described in Yuneva et al., 2007) and 10 mM [U-^{13}C]-
1069 glucose (Goss Scientific #CLM-1396-1). After 24 h incubation, cells were washed once with ice-cold
1070 PBS. Metabolites were extracted with adding 500 µl of ice-cold methanol, scraping, and transferring
1071 into tubes on ice. Dishes were then subsequently washed with 250 µl methanol and 250 µl water
1072 containing 2.5 nM of each nor-leucine and scyllo-inositol per sample as internal standards. Finally, 250
1073 µl of chloroform was added and samples were sonicated for 3 rounds (8 min each) at 4 °C. After
1074 centrifugation (18,000 g for 10 min at 4 °C), the upper polar fraction was collected and used for GC-
1075 MS analysis, while he protein pellets were dried, lysed using 62.5 mM Tris buffer (pH 6.8) containing
1076 2% SDS and used for protein quantification using BCA assay (Abcam). Briefly, the polar fraction was
1077 washed twice with methanol, derivatized by methoximation (Sigma, 20 µl, 20 mg/ml in pyridine) and

1078 trimethylsilylation (20 µl of N,O-bis(trimethylsilyl) trifluoroacetamide reagent (BSTFA) containing 1%
1079 trimethylchlorosilane (TMCS), Supelco), and analysed on an Agilent 7890A-5975C GC–MS system.
1080 Splitless injection (injection temperature 270 °C) onto a 30 m + 10 m × 0.25 mm DB-5MS + DG column
1081 (Agilent J&W) was used, using helium as the carrier gas, in electron ionization (EI) mode. The initial
1082 oven temperature was 70 °C (2 min), followed by temperature gradients to 295 °C at 12.5 °C/min and
1083 then to 320 °C at 25 °C/min (held for 3 min). Data analysis and peak quantifications were performed
1084 using MassHunter Quantitative Analysis software (B.06.00 SP01, Agilent Technologies). The level of
1085 labelling of individual metabolites was corrected for the natural abundance of isotopes in both the
1086 metabolite and the derivatization reagent. Abundance was calculated by comparison to responses of
1087 known amounts of authentic standards [60]. The data were further processed and visualised by
1088 MetaboAnalyst 4.0, using the Pathway Analysis module with the library of human SMPDB and the
1089 Metabolite Set Enrichment Analysis with the library of predicted metabolite sets [61].

1090

1091 **Lipidomics**

1092 Fibroblasts for lipid extraction were grown in 15 cm dishes in DMEM medium supplemented with 1%
1093 FBS until fully confluent. When confluent, cells were counted and about 10^6 cells were washed and
1094 lysed in 0.5 ml water on ice for 5 min. A Folch extraction was performed: 3ml of chloroform/methanol
1095 (2/1) was added to separate lipids in the organic phase and the solution was centrifuged at 4 °C for 30
1096 min. The organic phase was collected and stored in glass vials at -80 °C until the mass spectrometry
1097 analysis was performed. Before MS analysis, chloroform and methanol were evaporated and dried
1098 lipids resuspended in 150 µl MeOH/$CHCl_3$ 8:2. LC-MS measures were carried out by HPLC (Model 1100
1099 series; Hewlett-Packard) coupled to a quadrupole ion-trap mass spectrometer (Esquire-LCTM; Bruker,
1100 Bremen, Germany) equipped with an electrospray ion source (ESI), in both positive and negative ion-
1101 modes. Chromatographic separation of the lipids was carried out at 303 K on a C18 column by injecting
1102 5 µl of the 4 lipid raw extracts (3 biological replicates for each sample) into the column (Kinetex
1103 TMC18; length, 100 mm; particle size, 2.6 µm; internal diameter, 2.1 mm; pore size, 100 Å;
1104 Phenomenex, Torrence, CA, USA). The solvent system consisted of eluent A as CH_3OH/H_2O (7:3, v/v)
1105 containing 12 mM ammonium acetate, and eluant B as CH_3OH also containing 12 mM ammonium
1106 acetate. The linear gradient was run at a constant flow rate of 0.3 ml/min, and went from 30% B to
1107 100% B in 40 min. This was followed by the column wash using 100% B for 15 min, and then column
1108 re-equilibration under the starting conditions (i.e., 30% B). The nebuliser gas was high purity nitrogen
1109 at a pressure of 20 psi to 30 psi, at a flow rate of 6 L/min and 300 °C. The MS scan range was 13,000
1110 U/s in the range of 50 m/z to 1500 m/z, with a mass accuracy of ≈ 100 ppm. The ESI was operated in

1111 positive ion mode for the qualitative and quantitative analysis of lyso-GPC, GPC and SM, and both in
1112 positive and negative ion mode for glycerol-phospholipids classes GPI and GPE. For the structural
1113 assignment of the lipid species, the extracted ion chromatograms from the positive and/or negative
1114 ion full scan data were integrated using the DataAnalysis 3.0 software (Bruker Daltonik, Bremen,
1115 Germany). In particular, for PE, negative ion mode provided a good yield of molecular ions and
1116 information on the length and unsaturation index of the fatty acyl chains, while positive ion mode was
1117 used to confirm the correct assignment by analysis of the neutral loss of the polar head. The lipid
1118 quantitation was performed by integration of the extracted ion chromatograms (XIC), achieved
1119 through the proprietary software Bruker Daltonics esquireLC 4.5. Overall, the following lipid classes
1120 were detected: lysophosphatidylcholines (Lyso-GPC), glycerophosphatidylcholines (GPC), plasmenyl
1121 phosphatidylcholines (plasmenyl-GPC), sphingomyelins (SM), glycerophosphatidylethanolamines
1122 (GPE), plasmenly phosphatidylethanolamines (plasmenyl-GPE), glycerophosphatidylinositols (GPI),
1123 ceramides, and triacylglycerols (TAG), cholesteryl-esters and cholesterol. To compare across samples
1124 the results within a given lipid class, data were normalized with respect the total ion current (TIC) of
1125 this class (relative intra-class quantitation) whilst to compare the results among different lipid classes
1126 the corresponding signal areas were normalized to the total area of different classes in different runs
1127 (normalization to the relative protein amount leads to similar conclusions). Normalized MS data were
1128 further processed and visualised by MetaboAnalyst 4.0, using the Pathway Analysis module with the
1129 library of human SMPDB.

1130

1131 **Nile Red O imaging**

1132 Fibroblasts were plated on imaging coverslips and grown in DMEM medium supplemented with 1%
1133 FBS. After 24 hours, cells were incubated for 5 min with 0.1 µg/ml of Nile Red O (Sigma-Aldrich #72485)
1134 dissolved in imaging buffer [62]. Live cell imaging was performed on a Zeiss 880 confocal microscope,
1135 equipped with a 40x objective and exciting cells at 488 nm and collecting fluorescence longer than 530
1136 nm. Image analysis was performed using Fiji to evaluate the number of Nile Red positive puncta, likely
1137 lipid droplets, and their areas for each cell that was imaged.

1138

1139 **RNA-sequencing**

1140 Fibroblasts for RNA-sequencing were plated in 10 cm dishes with regular media (1 x 10^6 cells/dish) one
1141 day before RNA extraction. RNA extractions were performed using the RNeasy Mini Kit (Qiagen
1142 #74104). Concentrations and quality of RNA samples were quantified using NanoDrop (total RNA >250

1143 ng, A_{260}/A_{280} = 1.8-2.1, A_{260}/A_{230} > 1.7). RNA-sequencing was then performed at UCL Genomics and
1144 analysed by the SARTools R package [63]. The resulting datasets were further analysed by Ingenuity
1145 Pathway Analysis (IPA, Qiagen) with a threshold of FDR < 0.05 and visualised by Morpheus
1146 (https://software.broadinstitute.org/morpheus) for heatmaps and NetworkAnalyst 3.0 [64] for volcano
1147 plots and principal component analysis.

1148

1149 **Immunohistochemistry**

1150 For immunohistochemistry, muscle biopsies were fixed in phosphate buffered saline (PBS) and fixed
1151 in 4% paraformaldehyde (PFA), made in PBS, for 4-8 h at room temperature (RT). Following fixation,
1152 tissues were cryoprotected in 30% sucrose in Diethyl Pyrocarbonate (DEPC) treated PBS, embedded
1153 and frozen in a mixture of 15% sucrose /50% Tissue-Tek OCT (Sakura Finetek), and sectioned in the
1154 coronal plane at 20 µm using a Cryostat (Bright Instruments). Patient muscle biopsies sections were
1155 washed in PBS, blocked in a solution of 5% normal goat serum (Merck KGaA) (v/v) containing 0.1%
1156 Triton X-100 (v/v) (Merck KGaA) in PBS at RT for 2 h. They were first incubated in primary antibodies
1157 at RT overnight. The following antibodies were used: pan-AKT (1:200, Cell Signaling Technology
1158 #2920), phospho-AKT (p-AKT; 1:200, Abcam #ab81283), S6 (1:200), and phospho-S6 (1:200). Following
1159 incubation in primary antibodies, sections were washed in PBS, incubated in biotinylated anti-species
1160 secondary antibodies (1:250; Vector Laboratories) for 2 h. Sections were washed and incubated with
1161 bisbenzimide (10 min in 2.5 µg/ml solution in PBS; Merck KGaA). Images were collected using an SP2
1162 Leica confocal microscope (Leica Microsystems, UK). Sequential images were subsequently
1163 reconstructed using Metamorph imaging software (Universal Imaging Corporation, West Chester, PA).

1164

1165 **Immunofluorescence**

1166 For A549 cybrid cells, the cells were seeded at 1 x 10^5 cells per well in 6-well plates on 22 mm glass
1167 coverslips. On the day of the experiment, cells were replenished with regular media for 1 h to prevent
1168 starvation-induced autophagy. After 1 h, treatment conditions resumed either with or without 50 µM
1169 chloroquine for 6 h. The cells were then washed with PBS twice and fixed in 4% paraformaldehyde for
1170 20 mins at room temperature and permeabilised with 0.2% Triton X-100 in PBS for 5 min. Following
1171 washes with 0.2% Triton X-100 PBS, coverslips were incubated with primary anti-LC3B for
1172 autophagosomes/lysosomes (1:500) and anti-cytochrome c for mitochondria (1:200, BD Pharmingen
1173 #556432) antibodies in 3% BSA 0.2% Triton X-100 PBS at 4 °C overnight. The following day, cells were
1174 washed with 0.2% Triton X-100 PBS and incubated with Alexa Fluor 488-conjugated (goat anti-rabbit,

1175 1:200) and Alexa Fluor 647-conjugated (donkey anti-mouse, 1:500) secondary antibodies for
1176 visualisation of the lysosomes and mitochondria, respectively for 1 h. Following three PBS washes, the
1177 nucleus was counterstained using 5 µg/mL Hoechst 33342 solution diluted 1:2000 in 0.2% Triton X-
1178 100 PBS for 5 min. The coverslips were washed one final time with 0.2% Triton X-100 PBS and mounted
1179 on a glass slide using Fluoromount-G mounting medium (SouthernBiotech), stored at 4 °C until
1180 imaging. Imaging was performed with the LSM 880 microscope using 63x/1.40 oil immersion objective
1181 lens. For tricolour imaging, Hoescht 33342 was excited at 405 nm, Alexa Fluor 488 at 488 nm and Alexa
1182 Fluor 647 at 633 nm. Emitted fluorescence was collected at 410-480 nm, 500-650 nm and longer than
1183 660 nm. Images were acquired using Zen Black software (Carl Zeiss). Image acquisition parameters
1184 settings were maintained for all samples within the experimental set. The colocalisation coefficient
1185 (Pearson's R value) of 647 nm and 488 nm emission signals, LC3B and cytochrome c, was quantified
1186 using Coloc 2 in Fiji.

1187 For fibroblasts, cells were seeded at a density of 5 x 10^4 cells/well in 24 well plates on 10 mm
1188 coverslips. After 24h incubation, cells were treated with LY or RP for 4 weeks and 8 weeks respectively.
1189 After the long-term treatment, the cells were washed thrice with 1X PBS and fixed in 4%
1190 paraformaldehyde for 15 mins at room temperature and permeabilised with 0.1% Triton-X 100 for 15
1191 min in PBS. The cells were then washed and incubated with anti-MTCOI antibody (1:100, Abcam
1192 #ab14705) in 3% BSA for 1h at the room temperature followed by incubation with Alexa Fluor 488-
1193 conjugated secondary antibody for 1h at the room temperature. After antibody labelling, the
1194 coverslips were mounted on a glass slide using ProLong™ Gold Antifade mountant with DAPI and
1195 imaged using the confocal microscope as described above.

1196

1197 **TaqMan SNP genotyping for Single cell qPCR**

1198 Primers for distinguishing WT and the m.3243A>G mutant mtDNA were designed by submitting the
1199 region of the m.3243A>G mutation (~120 bp) to the website of online Custom TaqMan® Assay design
1200 tool (https://www.thermofisher.com/order/custom-genomic-products/tools/genotyping/) The
1201 Custom TaqMan SNP Genotyping Kit (Applied Biosystems #4332073) was ordered and prepared
1202 according to manufacturer instructions. For single cell sorting, cells were resuspended (1 x 10^6 cells/ml
1203 for A549 cybrid cells; 5 x 10^5 cells/ml for fibroblasts) in 1 ml PBS with 1% FBS, filtered through 70 µm
1204 mesh and then kept on ice. Sorting cells to 96-well PCR plates using BD FACS Aria Fusion was
1205 performed by Flow Cytometry Core Facility, Division of Medicine at UCL. Cells in 96-well plates were
1206 lysed with 2 µl of 0.2% Triton X-100 and kept in -80 °C immediately. For qPCR, TaqPath ProAmp Master

1207 Mix (Applied Biosystems #A30866) was mixed with primers of TaqMan SNP genotyping and added into
1208 96-well PCR plates to reach a final volume of 10 µl in each well. Thermo cycles were set according to
1209 manufacturer instructions. Mutant loads were determined by the ratio of mutant to total fluorescent
1210 intensity.

1211

1212 **QUANTIFICATION AND STATISTICAL ANALYSIS**

1213 All statistical analyses, unless otherwise stated in figure legends, were carried out using GraphPad
1214 Prism 8. To compare means between two groups, a two-tailed unpaired t-test was used for normally
1215 distributed data. One/two-way ANOVA with Tukey's multiple comparisons test was performed for
1216 multi-group (at least three) comparisons. Data are presented as graphs displaying mean ± s.d., of at
1217 least three independent biological replicates. Means of control samples on immunoblotting or
1218 immunofluorescence are typically centred at one (or 100%) to ensure easier comparisons unless
1219 otherwise noted. Differences were only considered to be statistically significant when the *p* value was
1220 less than 0.05. Estimated p values are either stated as the actual values or denoted by * $p < 0.05$, ** p
1221 < 0.01, *** $p < 0.001$, **** $p < 0.0001$.

1222 For detailed processing and statistical analysis of RNA sequencing, metabolomics and lipidomics,
1223 please find them in the previous section with the same subheadings.

1224 No statistical method was used to predetermine sample size, and replicates are shown in Figure
1225 legends. The investigators were not blinded to allocation during experiments and outcome
1226 assessment.

1227

1228 **REFERENCES**

1229 1. Gorman, G. S. *et al.* Prevalence of nuclear and mitochondrial DNA mutations related to adult
1230 mitochondrial disease. *Ann. Neurol.* (2015) doi:10.1002/ana.24362.

1231 2. Russell, O. M., Gorman, G. S., Lightowlers, R. N. & Turnbull, D. M. Mitochondrial Diseases:
1232 Hope for the Future. *Cell* **181**, 168–188 (2020).

1233 3. Craven, L., Alston, C. L., Taylor, R. W. & Turnbull, D. M. Recent Advances in Mitochondrial
1234 Disease. *Annu Rev Genomics Hum Genet* **18**, 257–275 (2017).

1235 4. Schon, E. A., DiMauro, S. & Hirano, M. Human mitochondrial DNA: roles of inherited and
1236 somatic mutations. *Nat Rev Genet* **13**, 878–890 (2012).

1237 5. Szczepanowska, J., Malinska, D., Wieckowski, M. R. & Duszynski, J. Effect of mtDNA point
1238 mutations on cellular bioenergetics. *Biochim. Biophys. Acta - Bioenerg.* **1817**, 1740–1746
1239 (2012).

1240 6. Stewart, J. B. & Chinnery, P. F. The dynamics of mitochondrial DNA heteroplasmy:
1241 implications for human health and disease. *Nat. Rev. Genet.* **16**, 530 (2015).

1242 7. Maeda, K. *et al.* Clinical Phenotype and Segregation of Mitochondrial 3243A>G Mutation
1243 in 2 Pairs of Monozygotic Twins. *JAMA Neurol.* **73**, 990–993 (2016).

1244 8. Picard, M. & Hirano, M. Disentangling (Epi)Genetic and Environmental Contributions to the
1245 Mitochondrial 3243A>G Mutation Phenotype: Phenotypic Destiny in Mitochondrial
1246 Disease? *JAMA Neurol.* **73**, 923–925 (2016).

1247 9. Valera-Alberni, M. & Canto, C. Mitochondrial stress management: a dynamic journey. *Cell*
1248 *Stress* **2**, 253–274 (2018).

1249 10. Kotiadis, V. N., Duchen, M. R. & Osellame, L. D. Mitochondrial quality control and
1250 communications with the nucleus are important in maintaining mitochondrial function and
1251 cell health()(). *Biochim. Biophys. Acta* **1840**, 1254–1265 (2014).

1252 11. Gilkerson, R. W. *et al.* Mitochondrial autophagy in cells with mtDNA mutations results from
1253 synergistic loss of transmembrane potential and mTORC1 inhibition. *Hum Mol Genet* **21**, 978–
1254 990 (2012).

1255 12. Morán, M. *et al.* Bulk autophagy, but not mitophagy, is increased in cellular model of

1256 mitochondrial disease. *Biochim. Biophys. Acta - Mol. Basis Dis.* **1842**, 1059–1070 (2014).

1257 13. Deus, C. M., Yambire, K. F., Oliveira, P. J. & Raimundo, N. Mitochondria–Lysosome Crosstalk:
1258 From Physiology to Neurodegeneration. *Trends Mol. Med.* **26**, 71–88 (2020).

1259 14. Plotegher, N. & Duchen, M. R. Mitochondrial Dysfunction and Neurodegeneration in
1260 Lysosomal Storage Disorders. *Trends Mol. Med.* **23**, 116–134 (2017).

1261 15. Cotán, D. *et al.* Secondary coenzyme Q10 deficiency triggers mitochondria degradation by
1262 mitophagy in MELAS fibroblasts. *FASEB J.* **25**, 2669–2687 (2011).

1263 16. Nigou, M., Parfait, B., Clauser, E. & Olivier, J. L. Detection and quantification of the A3243G
1264 mutation of mitochondrial DNA by ligation detection reaction. *Mol. Cell. Probes* **12**, 273–282
1265 (1998).

1266 17. Wang, J., Venegas, V., Li, F. & Wong, L. J. Analysis of mitochondrial DNA point mutation
1267 heteroplasmy by ARMS quantitative PCR. *Curr Protoc Hum Genet* **Chapter 19**, Unit 19 6
1268 (2011).

1269 18. Zhao, Y. *et al.* SoNar, a Highly Responsive NAD+/NADH Sensor, Allows High-Throughput
1270 Metabolic Screening of Anti-tumor Agents. *Cell Metab* **21**, 777–789 (2015).

1271 19. El-Hattab, A. W., Adesina, A. M., Jones, J. & Scaglia, F. MELAS syndrome: Clinical
1272 manifestations, pathogenesis, and treatment options. *Mol. Genet. Metab.* **116**, 4–12 (2015).

1273 20. Golla, S., Ren, J., Malloy, C. R. & Pascual, J. M. Intramyocellular lipid excess in the
1274 mitochondrial disorder MELAS. *Neurol. Genet.* **3**, e160 (2017).

1275 21. Manning, B. D. & Toker, A. AKT/PKB Signaling: Navigating the Network. *Cell* **169**, 381–405
1276 (2017).

1277 22. N'Diaye, E.-N. *et al.* PLIC proteins or ubiquilins regulate autophagy-dependent cell survival
1278 during nutrient starvation. *EMBO Rep.* **10**, 173–179 (2009).

1279 23. Suomalainen, A. & Battersby, B. J. Mitochondrial diseases: the contribution of organelle stress
1280 responses to pathology. *Nat Rev Mol Cell Biol* **19**, 77–92 (2018).

1281 24. Shpilka, T. & Haynes, C. M. The mitochondrial UPR: mechanisms, physiological functions and
1282 implications in ageing. *Nat. Rev. Mol. Cell Biol.* **19**, 109–120 (2018).

1283 25. Quirós, P. M. *et al.* Multi-omics analysis identifies ATF4 as a key regulator of the

1284 mitochondrial stress response in mammals. *J. Cell Biol.* **216**, 2027–2045 (2017).

1285 26. Deng, J. *et al.* RNA-seq profiling, and impaired autophagic process in skeletal muscle of
1286 MELAS. *Biochem. Biophys. Res. Commun.* **523**, 91–97 (2020).

1287 27. Gaude, E. *et al.* NADH Shuttling Couples Cytosolic Reductive Carboxylation of Glutamine with
1288 Glycolysis in Cells with Mitochondrial Dysfunction. *Mol. Cell* **69**, 581-593.e7 (2018).

1289 28. Molenaars, M., Daniels, E. G., Meurs, A., Janssens, G. E. & Houtkooper, R. H. Mitochondrial
1290 cross-compartmental signalling to maintain proteostasis and longevity. *Philos. Trans. R. Soc. B*
1291 *Biol. Sci.* **375**, 20190414 (2020).

1292 29. Mick, E. *et al.* Distinct mitochondrial defects trigger the integrated stress response depending
1293 on the metabolic state of the cell. *Elife* **9**, (2020).

1294 30. Garrido-Maraver, J. *et al.* Critical role of AMP-activated protein kinase in the balance between
1295 mitophagy and mitochondrial biogenesis in MELAS disease. *Biochim Biophys Acta* **1852**,
1296 2535–2553 (2015).

1297 31. Koromilas, A. E. & Mounir, Z. Control of oncogenesis by eIF2α phosphorylation: implications
1298 in PTEN and PI3K–Akt signaling and tumor treatment. *Futur. Oncol.* **9**, 1005–1015 (2013).

1299 32. Janssen, G. M. C. *et al.* The A3243G tRNALeu(UUR) mutation induces mitochondrial
1300 dysfunction and variable disease expression without dominant negative acting translational
1301 defects in complex IV subunits at UUR codons†. *Hum. Mol. Genet.* **16**, 2472–2481 (2007).

1302 33. Suen, D.-F., Narendra, D. P., Tanaka, A., Manfredi, G. & Youle, R. J. Parkin overexpression
1303 selects against a deleterious mtDNA mutation in heteroplasmic cybrid cells. *Proc. Natl. Acad.*
1304 *Sci.* **107**, 11835 LP – 11840 (2010).

1305 34. Kandul, N. P., Zhang, T., Hay, B. A. & Guo, M. Selective removal of deletion-bearing
1306 mitochondrial DNA in heteroplasmic Drosophila. *Nat. Commun.* **7**, 13100 (2016).

1307 35. Wojewoda, M., Duszyński, J. & Szczepanowska, J. NARP mutation and mtDNA depletion
1308 trigger mitochondrial biogenesis which can be modulated by selenite supplementation. *Int. J.*
1309 *Biochem. Cell Biol.* **43**, 1178–1186 (2011).

1310 36. de Andrade, P. B. M. *et al.* Diabetes-associated mitochondrial DNA mutation A3243G impairs
1311 cellular metabolic pathways necessary for beta cell function. *Diabetologia* **49**, 1816–1826
1312 (2006).

1313 37. Chen, Q. *et al.* Rewiring of Glutamine Metabolism Is a Bioenergetic Adaptation of Human
1314 Cells with Mitochondrial DNA Mutations. *Cell Metab.* **27**, 1007-1025.e5 (2018).

1315 38. Cappel, D. A. *et al.* Pyruvate-Carboxylase-Mediated Anaplerosis Promotes Antioxidant
1316 Capacity by Sustaining TCA Cycle and Redox Metabolism in Liver. *Cell Metab.* **29**, 1291-
1317 1305.e8 (2019).

1318 39. Raimundo, N. *et al.* Mitochondrial Stress Engages E2F1 Apoptotic Signaling to Cause
1319 Deafness. *Cell* **148**, 716–726 (2012).

1320 40. Hoxhaj, G. & Manning, B. D. The PI3K–AKT network at the interface of oncogenic signalling
1321 and cancer metabolism. *Nat. Rev. Cancer* **20**, 74–88 (2020).

1322 41. Castellano, B. M. *et al.* Lysosomal cholesterol activates mTORC1 via an SLC38A9–Niemann-
1323 Pick C1 signaling complex. *Science (80-.).* **355**, 1306 LP – 1311 (2017).

1324 42. Yambire, K. F. *et al.* Mitochondrial biogenesis is transcriptionally repressed in lysosomal lipid
1325 storage diseases. *Elife* **8**, e39598 (2019).

1326 43. Lin, Y.-F. *et al.* Maintenance and propagation of a deleterious mitochondrial genome by the
1327 mitochondrial unfolded protein response. *Nature* **533**, 416 (2016).

1328 44. Fessler, E. *et al.* A pathway coordinated by DELE1 relays mitochondrial stress to the cytosol.
1329 *Nature* **579**, 433–437 (2020).

1330 45. Guo, X. *et al.* Mitochondrial stress is relayed to the cytosol by an OMA1–DELE1–HRI pathway.
1331 *Nature* **579**, 427–432 (2020).

1332 46. Khan, N. A. *et al.* mTORC1 Regulates Mitochondrial Integrated Stress Response and
1333 Mitochondrial Myopathy Progression. *Cell Metab* **26**, 419-428 e5 (2017).

1334 47. Picard, M. *et al.* Progressive increase in mtDNA 3243A>G heteroplasmy causes abrupt
1335 transcriptional reprogramming. *Proc Natl Acad Sci U S A* **111**, E4033-42 (2014).

1336 48. McMillan, R. P. *et al.* Quantitative Variation in m.3243A > G Mutation Produce Discrete
1337 Changes in Energy Metabolism. *Sci. Rep.* **9**, 5752 (2019).

1338 49. Chae, S. *et al.* A Systems Approach for Decoding Mitochondrial Retrograde Signaling
1339 Pathways. *Sci. Signal.* **6**, rs4 LP-rs4 (2013).

1340 50. Civiletto, G. *et al.* Rapamycin rescues mitochondrial myopathy via coordinated activation of

1341 autophagy and lysosomal biogenesis. *EMBO Mol Med* **10**, (2018).

1342 51. Zheng, X. *et al.* Alleviation of neuronal energy deficiency by mTOR inhibition as a treatment
1343 for mitochondria-related neurodegeneration. *Elife* **5**, (2016).

1344 52. Haroon, S. *et al.* Multiple Molecular Mechanisms Rescue mtDNA Disease in C. elegans. *Cell*
1345 *Rep* **22**, 3115–3125 (2018).

1346 53. Johnson, S. C. *et al.* mTOR Inhibition Alleviates Mitochondrial Disease in a Mouse Model of
1347 Leigh Syndrome. *Science (80-.).* **342**, 1524 LP – 1528 (2013).

1348 54. Barriocanal-Casado, E. *et al.* Rapamycin administration is not a valid therapeutic strategy for
1349 every case of mitochondrial disease. *EBioMedicine* **42**, 511–523 (2019).

1350 55. White, H. E. *et al.* Accurate Detection and Quantitation of Heteroplasmic Mitochondrial Point
1351 Mutations by Pyrosequencing. *Genet. Test.* **9**, 190–199 (2005).

1352 56. Schindelin, J. *et al.* Fiji: an open-source platform for biological-image analysis. *Nat. Methods*
1353 **9**, 676–682 (2012).

1354 57. Rooney, J. P. *et al.* PCR based determination of mitochondrial DNA copy number in multiple
1355 species. *Methods Mol Biol* **1241**, 23–38 (2015).

1356 58. Rehman, J. *et al.* Inhibition of mitochondrial fission prevents cell cycle progression in lung
1357 cancer. *FASEB J.* **26**, 2175–2186 (2012).

1358 59. Yuneva, M., Zamboni, N., Oefner, P., Sachidanandam, R. & Lazebnik, Y. Deficiency in
1359 glutamine but not glucose induces MYC-dependent apoptosis in human cells . *J. Cell Biol.* **178**,
1360 93–105 (2007).

1361 60. Méndez-Lucas, A. *et al.* Identifying strategies to target the metabolic flexibility of tumours.
1362 *Nat. Metab.* **2**, 335–350 (2020).

1363 61. Chong, J., Wishart, D. S. & Xia, J. Using MetaboAnalyst 4.0 for Comprehensive and Integrative
1364 Metabolomics Data Analysis. *Curr. Protoc. Bioinforma.* **68**, e86 (2019).

1365 62. Listenberger, L. L. *et al.* Triglyceride accumulation protects against fatty acid-induced
1366 lipotoxicity. *Proc. Natl. Acad. Sci.* **100**, 3077 LP – 3082 (2003).

1367 63. Varet, H., Brillet-Guéguen, L., Coppée, J.-Y. & Dillies, M.-A. SARTools: A DESeq2- and EdgeR-
1368 Based R Pipeline for Comprehensive Differential Analysis of RNA-Seq Data. *PLoS One* **11**,

1369 e0157022 (2016).

1370 64. Xia, J., Gill, E. E. & Hancock, R. E. W. NetworkAnalyst for statistical, visual and network-based
1371 meta-analysis of gene expression data. *Nat. Protoc.* **10**, 823–844 (2015).

1372

1373 **ACKNOWLEDGEMENTS**

1374 We thank Ian Holt (Biodondostia Research Institute, San Sebastián, Spain) for sharing the A549 cybrid
1375 cell line with us, Michal Minczuk (MRC Mitochondrial Biology Unit, Cambridge, UK) for sharing the
1376 143B cybrid cell lines, Benoit Bilanges (UCL Cancer Institute) for invaluable discussions and guidance,
1377 Alice Giustacchini (UCL ICH) for help with single-cell analyses, Stephanie Carrington (Division of
1378 Neuropathology, UCL IoN) for sectioning the muscle biopsies, and Metabolomics STP of the Francis
1379 Crick Institute for assistance with GC-MS analysis. We also acknowledge The MRC Centre for
1380 Neuromuscular Diseases Biobank (supported by the National Institute for Health Research Biomedical
1381 Research Centres at Great Ormond Street Hospital for Children NHS Foundation Trust and at
1382 University College London Hospitals NHS Foundation Trust and University College London) for
1383 providing all patient-derived cells used in this study. NP was supported by Marie Sklodowska-Curie
1384 Individual Fellowship (Horizon 2020 Grant No. 653434) RDSP is supported by a Medical Research
1385 Council Clinician Scientist Fellowship (MR/S002065/1). GS is supported by Telethon GGP16026 and
1386 CRUK Pioneer Award C28472/A29264. MY is supported by the Francis Crick Institute which receives
1387 its core funding from Cancer Research UK (FC001223), the UK Medical Research Council (FC001223),
1388 and the Wellcome Trust (FC001223). We also thank Action Medical Research for funding the early
1389 stages of this work and the Taiwan government for funding CYC's PhD Fellowship.

1390